INVESTIGATION INTO WATER-SOLUBLE PERYLENE DIIMIDES FOR THIN FILM FORMATION

by

COREY R. WEITZEL

B.S. University of Northern Colorado, 2004

A THESIS

Submitted in partial fulfillment of the requirements for the degree

MASTER OF SCIENCE

Department of Chemistry
College of Arts and Sciences

KANSAS STATE UNIVERSITY
Manhattan, Kansas

2008

Approved by:

Major Professor
Dan A. Higgins

Abstract

Three water-soluble perylene diimides (PDIs) were investigated to examine differences in their thin film forming properties. The PDI thin films investigated in this thesis are formed in an electrostatic-self-assembled (ESA) layer-by-layer (LBL) process by the use of a dip coater. The three PDIs employed are sodium bis (sulfonatopropyl) perylene diimide ($PDISO_3^{2-}$), bis (trimethylammonioethyl) perylene diimide diiodide ($PDIDI^{2+}$), and N-(butoxypropyl)-N'-(2-(N,N,N-trimethylammonio)-ethyl) perylene-3,4,9,10-tetracarboxylic diimide iodide (C_7OPDI^+). Thin films were made by alternately depositing the PDIs with counter polyelectrolyte (PEs). The PEs employed were poly(diallyldimethylammonium chloride) ($PDDA^+$) and poly(acrylic acid) (PA^-), depending on the charge of the PDI. PDIs were determined to be aggregated in all three PDI precursor solutions. The fraction of PDI aggregated in each was found to be 0.972, 0.903, and 0.993, for the $PDISO_3^{2-}$, $PDIDI^{2+}$, and C_7OPDI^+, respectively. The C_7OPDI^+ solution was the most aggregated only having one charge group, which makes it more hydrophobic. Thin films prepared from the solutions all displayed an absorbance spectrum similar to the aggregated form.

All the composites displayed linear growth in film thickness and fiber width with bilayer number. However, the three composites gave unique surface morphologies. The $PDISO_3^{2-}$•$PDDA^+$ composite was found to incorporate highly curled intertwined fibers compared to the $PDIDI^{2+}$•PA^- composite, where the fibers were not intertwined. The fiber structure was found to change after 15 bilayers. This change in morphology was attributed to the fibers grafting together and overlapping causing the loss of original fiber structure. The two symmetric composites differed in the film thickness with the $PDISO_3^{2-}$•$PDDA^+$ being thicker than the $PDIDI^{2+}$•PA^- composite. This was attributed to the molecular weights (MW) of the polyelectrolytes investigated during thin film deposition, with the $PDDA^+$ having a much higher MW. C_7OPDI^+•PA^- thin film composite had a film thickness approximately equal to the $PDISO_3^{2-}$•$PDDA^+$ composite, indicating precursor aggregation also influences deposition rate. The C_7OPDI^+•PA^- composite incorporated wavy thin fibers that appeared aligned in the dipping

direction. This alignment was visible for bulk samples in UV-vis absorption dichroism studies. The alignment was parallel to the dipping direction of the substrate.

Table of Contents

List of Figures

List of Equations

Acknowledgements

I would like to thank my advisor Dan A. Higgins for his patience and help through this entire process. I appreciate his understanding over the last several years. He has been a great motivation. I would like to express my appreciation to my committee members in Christopher T. Culbertson and Kenneth J. Klabunde.

The research done throughout my time here would not have been accomplished if not for many people. I give thanks to Richard Bachamp, Tobe Eggers, and Ron Jackson for their work in building the Dip Coater involved in the entire research project. I would like extend my appreciation out to my co-workers and others in my lab, especially Tom Everett. Most of all I thank my family and friends back in Colorado for listening and encouraging me.

The thesis work was supported by funding from National Science Foundation (Project # DMR-0076169, CHE-0404578) and Office of Naval Research (N00014-02-1-0584).

CHAPTER 1 - Introduction

1.1. Organic Semiconductors:

Small molecule organic semiconductors first started to be examined for electronic devices when organic dyes were incorporated into photovoltaic cells.[1,2,3] This resulted in the finding that organic semiconductors have interesting properties, such as ease of deposition, high quantum yields, and the ability to tailor electronic properties. These findings have lead to expanded research into this area. This subject has rapidly expanded and experienced increase funding over the last decade. Some of chief causes for the increase in interest are tied the rising cost of oil and other energy sources.

Solar energy is a possible way to reduce dependence on foreign oil and other sources of non-renewable energy. The problem right now is that the cost of solar panels is too high, with a cost per unit of $740 and a minimum order requirement of 12 panels.[4] Further research into semiconducting materials is for the reduction in the price of the materials. Reduction of cost is the reason for the continued effort to fully understand and improve the efficiencies of organic semiconducting materials.

Alteration of the base structure of organic semiconducting materials is often carried out for improved devices. The base structure of the organic semiconductors can be altered by the addition of different functional groups. There are several reasons for the alteration of the base structure, including for the purpose of changing the electronic properties, solubility of the precursors, and changing the morphology of the films.[5,6,7] Choice of functional groups added to the base material can change the electronic properties to a more favorable range. Solubility properties of organic semiconductors are changed to increase solubility in more common solvents. Current solvents are toxic and have negative effects on the environment. The morphology has an importance for organic photovoltaics since the films created need to be free of holes in order to prevent electrical shorts from occurring. The ability to modify organic semiconductors is part of the reason for the growing interest in organic semiconducting materials.

Organic semiconducting materials have certain advantages over inorganic semiconductors. An example is the ease of film deposition results in materials that are cheaper

to process. Cheaper processing is a result of lower temperatures used for deposition, thus flexible plastic substrates can be produced.[8,9] However, thin films may also be created from solution. The cost of organic starting materials is also lower. All the afore mentioned reasons make the cost lower for the manufacturing of the materials.

Organic semiconducting materials have some similar characteristics to their inorganic counterparts in behavior. Two types of materials exist with one being referred to as the hole-transporting layer and the other as the electron-transporting layer, which can be called p-type and n-type layers respectively. The type of characteristics shown in the organic semiconducting molecules can be changed by the addition of electron withdrawing groups like fluorine with a change from p-type to n-type observed.[10] All organic semiconducting materials contain π-electrons and a high degree of conjugation in their structure. The better working materials have a large amount of π-bonds present in the films.

Organic semiconducting materials have to be deposited into a thin film to find truly useful applications for them. Thin film morphology and growth mechanisms need to be fully understood along with its relationship to the electronic properties. Organic semiconductors fall into two categories in either polymer or molecular semiconductors.

1.2. Organic Semiconducting Polymers:

Organic semiconducting polymers have been incorporated in semiconducting materials with a few examples being: thiophene, phenylenevinylene, polyolthiophenes, and polyanilines.[11,12,13,14] Thiophene derivative is an example of a p-type polymer where promise is held for use in applications such as organic thin film transistors (OTFTs).[15] Thiophene and polyaniline derivatives can both be purchased commercially with one supplier being American Dye Source. [16] Commercially sold derivatives of these compounds are able to be dissolved in a wide variety of solvents. Several of the commercially obtained thiophene derivatives do in fact show the ideal quality of being water-soluble.[16] Water-solubility is brought about by addition of a substituent to the thiophene polymer. An unintended consequence in adding branches to the polymer chain is the loss of the desired π-π overlap.[17] Loss of π-stacking is the result of the polymers twisting up into coiled structures.

Substituents attached to the surface may act to increase the electron withdrawing capability, an example is fluorine.[18] Tuning of the electronic properties can occur by attachment

of a conjugated ring in the branched substitute. Their ability to be tuned makes them an excellent material for applications where tailoring the optical characteristics is desired. The thesis work here will not cover semiconducting polymers, thus no more time will be spent discussing them.

1.3. Molecular Organic Semiconductors:

1.3.A. P-type:

Molecular organic semiconductors consist of phthalocyanine, C_{60}, phorphyrins, pentacene, perylene, and derivatives of these. The majority of molecular organic semiconductors are p-type in behavior, while a few can be considered n-type. A large amount of research has been put into p-type molecular organic semiconductors. P-type material that has experienced the greatest success is a pentacene, which in an organic thin film transistor (OTFT) has a highly desirable μ_{fet} of 1 $cm^2\ V^{-1}\ s^{-1}$.[19,20,21,22,23] The result is equal to or greater than the values found for amorphous silicon.[20,21,22,23] A complete understanding of how the film morphology affects the high mobility has not been obtained for this or other molecular semiconductors.

Research involving p-type materials has begun to move to incorporation with n-type containing materials for uses in photovoltaics. In photovoltaics their needs to be both a p and n type layer present for higher efficiencies to be observed. Photovoltaics can be in the form of a single layer, dual layer, or blended layer device. A dual layer device has both n and p type materials, which have higher efficiencies. The development of better thin films involving the complimentary n-type materials requires further investigations.

1.3.B. N-type non PDIs:

Early research into molecular semiconductors showed the need for n-type organic semiconducting materials along with p-type to obtain higher efficiency in photovoltaic and light emitting diodes.[24,25] Research into n-type molecular semiconductors has increased because the desire for higher efficiencies matching those observed in p-type materials. The problem with n-type materials is that fewer exist and many suffer degradation in atmospheric conditions.[26,27] The degradation problem is well noted along with how n-type materials suffer from low field effect mobilities.[28,29,30,31,32] Several exceptions to the atmospheric degradation exist with a metalophthalocyanines and 4,4'-bis[(6,6'-diphenyl)-2,2-difluoro-1,3,2-dioxaborine in thin films

as prime examples where useful devices have been made that are air stable.[33,34] In attempts to increase the field effect mobilities, electron withdrawing groups are often attached as derivatives to the central molecule. The most commonly researched class of n-type molecular semiconducting materials is perylene diimides (PDIs).

1.3.C. PDI:

PDIs are already heavily used in today's society where they're found as pigments in car paint and as dyes for other applications. PDIs are excellent molecules to study for various reasons. The biggest reason is PDIs display excellent electron transport.[35] PDIs have been involved in investigations for enhanced donor acceptor systems. PDIs have been investigated for a variety of solution electron transfer systems with dendrimers incorporating PDIs.[36,37] PDIs display a large two photon absorption cross section, which results in possible photonic applications.[38] Devices have been investigated with PDI demonstrating organic transistors and hybrid photovoltaic systems.[39,40]

PDIs display excellent liquid crystalline properties of self-assembly. Self-assembly is a direct consequence of the conjugated core of the various PDIs. The conjugated core allows for PDI to self-assemble spontaneously with N-substituted PDIs. The edge on orientation is considered important when self-assembly is observed in the liquid crystalline phase.[41,42] PDIs were found to display liquid crystal behavior by the addition of shorter linear chains compared to those required for other organic semiconducting materials where a greater number of chains was required.[43] A liquid crystal with a PDI derivative has shown electron mobilities higher than amorphous silicon.[44] A range of N-alkyl substituted PDIs have displayed liquid crystalline behavior. PDI compounds have created liquid crystals where liquid crystalline phases show smectic and columnar discotic structures.[45] Liquid crystallinity has been demonstrated in a water-soluble PDI, where a combination nematic and isotopic region exist in a narrow region.[46]

Perylene 3,4,9,10-tetracarboxylic dianhydride (PTCDA) is shown in figure 1. The two positions where modifications are carried out are shown in figure 1. The positions on the sides are the bay positions. The position at both of the dianhydride ends is where substitution with a primary amine could occur. A wide variety of substituents have been attached to the dianhydride ends via primary amine substitution.[47,48,49] These derivatives comprise everything from straight chains, branched carbon chains, phenyl groups, and a wide assortment of other functional

groups. These derivatives lead to the so called crystal chromic effect where different derivatives substituted at the N-alkyl ends show identical absorption spectra when in the free molecule non-aggregated state.[47] However, there exists a difference in the absorption and emission spectra when present in the molecular aggregated state.[50] The spectra differences are caused by the different attachments to the nitrogen atom, which results in changes to the solid state packing and shifts electronic properties when in thin films.[51,52]

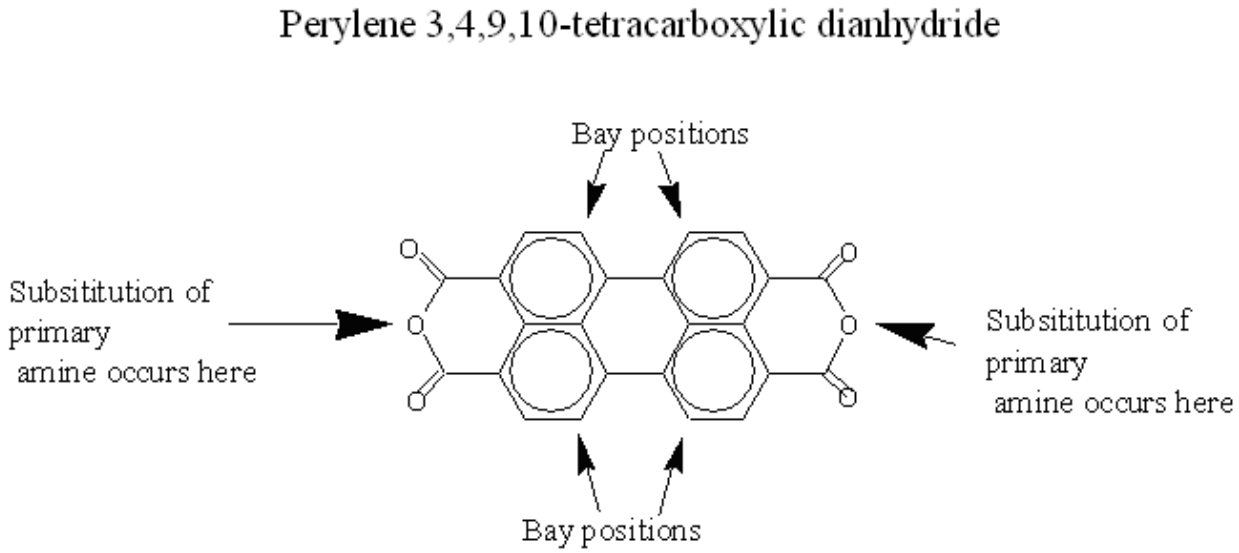

Figure 1.1. PTCDA

PTCDA displaying the positions where derivatives are added.

PTCDA suffers from the same problem as a lot of the other organic semiconductors in not being very soluble in common solvents. The solvents where PTCDA is soluble tend to be harmful to the environment and negatively affect the health of living organisms.[53] A diperfluorophenyl derivative of PTCDA is a prime example of being soluble in harsh solvents such as THF, acetone, chloroform, toluene, and dioxane.[6] The authors of the paper wrote about the increased solubility in the above mentioned solvents. Several groups have synthesized water-soluble derivatives of PTCDA, thus solving the solubility problem.

With most of the PTCDA derivatives being alkyl substituted, it should be noted that one of the few water-soluble PDIs, which has drawn attention, is bay-substituted.[54] The solubility was obtained by two additions to PTCDA base structure. First the perylene core is distorted by the substitution at the bay position, which increases the solubility. Second, the addition of charged groups onto the substituted aromatic rings is responsible for the water-solubility. The

two compounds were found to form weakly interacting species in water.[55] Bay-substituted PDIs have shown energy transfer efficiency differences depending on type of charge group attached to the PDI.[55] Dual layer films of these bay-substituted PDI showed efficient energy transfer through the moieties when films contained both the positive and negative charged groups.[56]

The rest of the reported water-soluble PDIs have N-alkyl substituted derivatives. An example is a dual cationic PDI formed by a substitution reaction with a primary amine. Dual charged cationic PDI exhibits self-organization with mechanically induced orientation and order transfer processes.[57] Thus, there is controlled orientation in the films. The mechanical alignment involved the use of a home built coating apparatus to obtain the organization.[58] The liquid crystal interface pressed against the substrate created organization within the film. Thin film organization is of importance in the understanding and control for functional applications to be reached.

The two earlier discussed methods for the formation of thin films from water-soluble PDIs relied on electrostatic attraction with the use of ammonium salt groups. Another type of water-soluble PDI also took advantage electrostatic attraction by use of phosphate-zirconium linkage to form thin films.[59] Phosphate functionalized PDIs were found to be present in various states depending on the solvent used. Where water, ethanol, water/ethanol, DMSO, and 10 mM CTAB are used the resulting aggregation state were a dimer, higher aggregate, monomer, dimer, and monomer respectively.[59] The CTAB was a surfactant that was effectively able to form micelles containing the PDI in solution. When the CTAB was present above critical micellar concentrations evidence of just the monomer being present in solution was obtained. CTAB solutions with sub-critical micellar concentrations resulted in larger aggregates. Thin films made with phosphate functionalized PDI were found to display no fluorescence as a result of stacking of the PDIs in thin films. The phosphate functionalized PDIs were investigated for the purpose of a mixed heterojunction with mixed success.[60]

1.4. Thin Film Formation:

Organic semiconducting materials can form various thin films and other useful structures such as nanofibers. Thin films are made by many methods, such as spin casting, vacuum deposition, thermal evaporation, sputtering, Langmuir Blodgett methods, dip coating, and solution deposition. The type of methods involved in thin film formation determines the

thickness and the roughness of the thin film's surface. All the methods available for creating the thin films have several variables that can be adjusted. Concentration of the solutions used in the various methods affects how much material goes down. The temperature employed when thermal evaporation is used in forming thin films could change the film morphology.[61] Thermal evaporation has advantages in that it usually leads to high purity materials, large grain size, and crystalline materials.[27] Structure of the starting materials does affect the order in the films based on the chain length and chain orientation, as has been demonstrated with C_{60} derivatives.[7]

1.4.A. Layer by Layer Formation:

The formation of thin films using layer-by-layer (LBL) methods has a wide range of advantages and has been implemented by numerous research groups. LBL methods usually involve electrostatic-self-assembly (ESA) where oppositely charged materials are deposited. The first advantage is a way to control the thickness of the film composite. The second advantage of LBL methods is the ability to introduce multifunctionality into the films by the changing the materials deposited in the various layers.[62] Photocurrent action response has been reported to increase with bilayer number.[63]

LBL methods predominantly employ solutions from which the starting materials can be deposited. Precursor solutions have been used with various techniques to form LBL films. The solvents involved can be evaporated off. Many of the LBL studies involve the deposition of molecular organic semiconductor molecules onto the surface in the form of aggregates. However, thin films created may not involve aggregates depositing on the surface.[64] When solution deposition is involved a rinse solution is required between the precursor solutions, these rinse solutions have the same solvent as the one in the precursor solutions. When the solvents used in the various LBL precursor solutions happen to be of different solvents, several different rinse solutions could be required between each of the precursor solutions.[65] Using several rinse solutions prevents any solvent getting in the deposition solutions, which may change the state of the molecules from aggregated to monomer.

A unique way to deposit LBL films involves spin casting of the various organic layers with charge reversal at the surface, thus allowing for subsequent layer formations. This unique spin casting method has provided a way to create thin films in a linear manner even without alternating between charged molecules, as reported by Chiarelli et al.[66] The method invented

was found to give a thickness up to 60 nm thick for a dendrimer and PAZO combination examined.[66] Spin casting is not readily involved with most LBL deposition systems. The majority of thin film deposition methods involve immersion of the substrate into a solution containing the material desired for deposition, one such method involves the use of a dip coater.

Dip coating procedures involved in thin film formation can be automated, thus allowing for scale up. Scale up is why thin films made by the use of a dip coater are of interest. The factors, which can be varied, are deposition time, withdrawal and insertion rates, number of layers deposited, materials used, and concentration of the precursor solutions. Layer formation is effectively demonstrated in how after a certain time in the precursor solution the absorbance increase leveled off as an indication that equilibrium had been reached.[55] One of the factors determining how fast a layer forms is the concentration of the precursor solution. A greater amount of material available to deposit increases the chance of bonding occurring on the substrate. Many molecular organic semiconductors deposit into thin films in the form of aggregates.[59,67] The presence of high ionic strength can have the effect of creating larger aggregates which leads to faster thin film formation. Formation of aggregates in solution depends on the material being deposited and the solvent used in the deposition. Increased ionic strength does not guarantee aggregates present in solution, but does effectively act as a way for increased thin film deposition. LBL film deposition is an ideal system if the thickness of the films needs to be controlled, as the thickness depends on the number of layers deposited.

1.4.B. Materials Involved in Layer-by-Layer Formation:

Organic semiconducting materials formed in electrostatic-self-assembled (ESA) LBL processes have involved a wide variety of materials. ESA-based LBL studies have been demonstrated to work with carbon nanotubes where Indium was melted on the surface to facilitate deposition of the nanotubes.[68] The nanotubes had charged polyelectrolytes adsorbed to the surface to facilitate the LBL formation by alternating between charged solutions. Evidence exists that PDIs with appropriate counter polyelectrolyte (PEs) form thin films via the ESA-based LBL process.[55] LBL solution methods do not just have to involve organic materials; zirconium and ruthenium metals have been incorporated into films.[59,60,65]

Several variations of water-soluble PDIs have been employed for LBL deposition of composite films. The water-soluble bay-substituted PDIs showed excellent LBL growth.[55] Bay-

substituted PDIs could effectively be used for the formation of LBL structure without the use of polyelectorlytes.[56] LBL formation reported by Tang is the result of electrostatic attraction. Thin film composites observed had strong evidence of fluorescence quenching indicating stacking of PDIs in the solid state.[56] The other water-soluble investigations involved PDIs with phosphate linkage displayed linear absorbance and thickness increase with bilayer number.[59] This LBL growth of two structurally different PDIs demonstrates how LBL methods have effectively grown thin films from water-soluble PDIs.

1.5. Film Structure:

Thin film growth can be monitored by several instrumental techniques. First, thin film growth can be tracked by the use of UV-vis spectroscopy. Second, elliposometry can monitor the growth of thin films' thickness. Third, the samples surface can be scratched with a razor to remove the thin film composite down to the substrate. Then, atomic force microscope could be used to image the area where the scratch is located on the film. The image obtained could then have a computer program run to determine the film's thickness.

The composite thin films surface morphology is of importance. The thin films should be free of holes for prevention of electrical shorts in photovoltaics. Roughness of the interface between the p and n layers needs to be controlled. Order observed within the films dictates performance in photovoltaics. A wide variety of instrumentation has been employed to examine these various surface features for organic semiconductor films. Instrumental techniques for characterization of the surface morphology can increase the understanding of the crystal packing structure present. Crystal packing structure has significance in the films photo-response characteristics.[69] The most common instruments employed to examine thin films on the microscale are transmission electron microscopy (TEM), scanning tunneling microscopy (STM), scanning electron microscopy (SEM), and atomic force microscopy (AFM). TEM, SEM, and STM involve a current passing through the sample making these techniques not useable for all samples.

The most common instrument involved in examination of the surface morphology is AFM. AFM has the advantage of the films not having to be conductive, thus any type of substrate and material can be imaged. AFM imaging is possible by measuring the change in the oscillation of a cantilever with a laser. Images obtained can help determine the average surface

roughness of the composite films. Also, distinct features can be readily observed based on the height differences between the feature and surface.[67] The sharpness of the tip has a direct relationship to the quality of the image obtained.

Instrumental techniques exist where not only the surface features can be imaged, but also the fluorescent properties of the structures can be probed. Near-field scanning optical microscopy (NSOM) is one such technique. Thin films having highly fluorescent molecules incorporated in the composites can have the fluorescence intensities measured, along with the structural properties of the films. PDI fluorescent nanobelts have been observed by fluorescence microscopy and NSOM.[70] Insights gained with NSOM give the possibilities that PDIs can be used in orientation-sensitive applications.[71] The size of crystals in mixed films of PDI and phthalocyanine with NSOM was obtained. Other microscopy techniques exist where the morphology is not imaged but the fluorescence intensity at various locations is obtained with confocal fluorescence microscopy. Confocal fluorescence microscopy gives valuable information regarding the distribution of the fluorescent compounds on the surface.

1.6. Present Work:

The work presented in this thesis involves the effects that several different water-soluble PDIs have on thin film formation. This investigation aims to understand how different N-alkyl substituted water-soluble PDIs effect thin film growth. The PDIs investigated here are either symmetrically charged (cationic and anionic) or asymmetrically charged. The symmetric PDIs explored will be sodium bis (sulfonatopropyl) perylene diimide ($PDISO_3^{2-}$) and bis (trimethylammonioethyl) perylene diimide diiodide ($PDIDI^{2+}$). The asymmetric PDI examined is N-(butoxypropyl)-N'-(2-(N,N,N-trimethylammonio)ethyl) perylene-3,4,9,10-tetracarboxylic diimide iodide (C_7OPDI^+). Polyelectrolytes (PEs) used are poly(acrylic acid) (PA^-) and poly (diallyldimethylammonium chloride) ($PDDA^+$), depending on the charge of the PDI. In this thesis, the thin films will be created in an electrostatic-self-assembly (ESA) system with layer-by-layer (LBL) thin film growth. ESA-based LBL growth can easily be accomplished by the charge reversal carried out at the surface where each layer results in charge reversal. Thin films of the water-soluble PDIs and PEs will be prepared with ESA-based LBL methods. Two polyelectrolytes have previously been investigated in ESA-based LBL studies found in the

literature.[66,72,73] $PDDA^+$ and PA^- have shown uniform linear growth by LBL methods previously.[74]

Thin films of PDIs and PEs will be constructed by application of a dip coater. The Higgins group with water-soluble PDIs has used both dip coating and drop casting in the past.[67,75] The features observed in the thin films surface morphology will be examined, along with the thin film growth. Morphology of the surface features will be imaged since a relationship with future performance in devices to morphology exists.[76] With a complete understanding of how thin film growth varies by various water-soluble PDIs will lead to better future applications.

A possible system to obtain organization of the thin films surface fibers will be examined in the latter part of this work. This investigation was brought about by the observation that $C_7OPDI^+ \bullet PA^-$ composite showed signs of alignment in dip coated films. Alignment of fibers is important since aligned nanofibers have several possible uses in nanowires, organic thin film transistors (OTFTs), and dichroics. Control of the nanofiber growth in a directional manner can lead to electronic applications such as nanowires. Alignment of the nanofibers could be employed in efficient organic field effect transistors, where control of packing increases performance.[69] High order in OTFTs results in reduction of unwanted characteristics such as leakage currents.[77] Alignment of fibers could lead to increased exciton diffusion length, already demonstrated with PDI.[78,79,80] Films displaying a high degree of order may be used as dichroics. An example is a water-soluble PDI where a dichroic ratio of 6 was displayed.[81]

References

[1] Weinberger, B. R.; Gau, S. C.; Kiss, Z. *Appl. Phys. Lett*. **1981**, 38, 555.

[2] Glenis, S.; Horowitz, G.; Tourillon, G.; Garnier, F. *Thin Solid Films* **1984**, 111, 93.

[3] Marks, R. N.; Halls, J. J. M.; Bradley, D. D. C.; Friend, R. H.; Holmes, A. B. *J. Phys. Condens. Matter*. **1994**, 6, 1379.

[4] www.solarpanelstore.com

[5] Ling, M.; Bao, Z.; Erk, P.; Konenemann, M.; Gomez, M. *Appl. Phys. Lett.* **2007**, 90, 093508.

[6] Chen, H. Z.; Shi, M. M.; Aernouts, T.; Wang, M.; Borghs, G.; Heremnas, P. *Sol. Energy Mater. & Solar Cells* **2005**, 87, 521.

[7] Chikamatsu, M.; Itakura, A.; Yoshida, Y.; Azumi, R.; Kikuchi, K.; Yase, K. *J. Photochem. And Photobiology A: Chem.* **2006**, 182, 245.

[8] Bao, Z.; Rogers, J. A.; Katz, H. E. *J. Mater. Chem*. **1999**, 9,1998.

[9] Rogers, J. A.; Bao, Z.; Katz, H. E.; Dodabalapu, A. *Thin Film Transistors* **2003**, 377.

[10] Kikuzawa, Y.; Mori, T.; Takeuchi, H. *Org. Lett.* **2007**, 9, 2007.

[11] Vusser, S.; Schols, S.; Steudel, S.; Verlaak, S.; Genoe, J.; Oosterbaan, W.; Lutsen, L.; Vanderzande, D.; Heremans, P. *Applied Physics Letters* **2006**, 89, 223504.

[12] Yoon, M. H.; Kim, C.; Facchetti, A.; Marks, T. *J. Am. Chem. Soc.* **2006**, 128, 12851.

[13] Cloi, H. J.; Kim, J. W.; To, K. *Synthetic Metals* **1999**, 101, 697.

[14] Yakuphanoglu, F.; Liu, H.; Xu, J. *J. Phys. Chem. B* **2007**, 111, 7535.

[15] Chang, J.-F.; Sun, B.; Breiby, D. W.; Nielsen, M. M.; Sölling, T. I.; Giles, M.; McCulloch, I.; Sirringhaus, H. *Chem. Mater.* **2004**, 126, 3378.

[16] www.adsdyes.com

[17] Rasmussen, S. C.; Straw, B. D.; Hutchinson, J. E. (**1999**) *Semiconducting Polymers Tuning the Extent of Conjugation in Processable Polythiophenes Through Control of Side Chain Density and Regioregularity*. In B. R. Heish, Y. Wei *Semiconducting Polymers Applications, Properties, and Synthesis* (p. 347). Oxford: Oxford Univ. Press

[18] Wheland, R. C.; Gilson, J. L. *J. Am. Chem. Soc*. **1976**, 98, 3916.

[19] Nelson, S. F.; Lin, Y. Y.; Gundlach, D. J; Jackson, T. N. *Appl. Phys. Lett*. **1999**, 72, 1895.

[20] Gundlach, D. J.; Klauk, H.; Sheraw, C. D.; Kuo, C. C.; Huang, J. R.; Jackson, T. N. *1999 Tech. Dig. –Int. Electron Devices Meet.* **1999**, 111.

[21] Kluak, H.; Halik, M.; Zshieschang, U.; Schmid, G.; Radlik, W.; Weber, W. *J. Appl. Phys.* **2002**, 92, 5259.

[22] Kelly, T. W.; Broadman, L. D.; Dunbar, T. D.; Muyres, D. V.; Pellerite, M. J.; Smith, T. P. *J. Phys. Chem. B* **2003**, 107, 5877.

[23] Kelly, T. W.; Muyres, D. V.; Baude, P. F.; Smith, T. P.; Jones, T. D. *Mater. Res. Soc. Symp. Proc.* **2003**, 771, L6.5.1

[24] Tang, C. W.; *Appl. Phys. Lett*. **1986**, 48, 183.

[25] Tang, C. W.; Van Slyke, S. A. *Appl. Phys. Lett*. **1987**, 51, 913.

[26] De Leeuw, D. M.; Simenon, M. M. J.; Brown, A. R.; Einerhand, R. E. F. *Synth. Met*. **1997**, 87, 53.

[27] Newman, C. R.; Frisbie, C. D.; da Silva Filho, D. A.; Bredas, J. L.; Ewbank, P. C.; Mann, K. R. *Chem. Mater*. **2004**, 16, 4436.

[28] Brown, A. R.; Leeuw, D. M.; Having, E. E.; Pomp, A. *Synth. Met*. **1994**, 68, 65.

[29] Laquindanum, J. G.; Katz, H. E.; Dodabalpur, A; Lovinger, A. *Synth. Met.* **1996**, 118, 11331.

[30] Katz, H. E.; Johnson, J.; Lovinger, A. J.; Wenjie, L. *J. Am. Chem. Soc*. **2000**, 122, 228.

[31] Facchetti, A.; Mushrush, M.; Katz, H. E.; Marks, T. *J. Adv. Mater*. **2003**, 15, 33.

[32] Chen, X. L.; Bao, Z.; Batlogg, B.; Schon, J. H.; Lovinger, A. J.; Lin, Y.; Crine, B.; Dodabalpur, A. *Appl. Phys. Lett*. **2001**, 78, 228.

[33] Bao, Z.; Lovinger, A. J.; Brown, J. *J. Am. Chem. Soc*. **1998**, 120, 207.

[34] Sun, Y.; Rojde, D.; Liu, Y.; Wan, L.; Wang, Y.; Wu, W.; Di, C.; Yu, G.; Zhu, D. *J. of Mater. Chem*. **2006**, 16, 4499.

[35] Horowitz, G.; Kuoki, F.; Spearman, P.; Fichou, D.; Nogues, C.; Pan, X.; Garnier, F. *Adv. Mater. Commun.* **1996**, 8, 242.

[36] Rybtchinski, B.; Sinks, L. E.; Wasielewski, M. R. *J. Am. Chem. Soc.* **2004**, 126, 12268.

[37] Shibano, Y.; Umeyama, T.; Mantano, Y.; Tkachenko, N. V.; Lemmetyinen, H.; Imahori, H. *Organic Letters* **2006**, 8, 20, 4425.

[38] Corrêa, D. S.; Oliveira, S. L.; Misoguti, L.; Zillio, S. C.; Aroca, R. F.; Constantino, C. J. L., Mendonca, C.R. *J. Phys. Chem. A* **2006**, 110, 6433.

[39] Yoo, B.; Madgavker, A.; Jones, B.A.; Nadkarmi, S.; Facchetti, A.; Dimmler, K.; Wasielewski, M. R.; Marks, T. J.; Dodabalapur, A. *Electron Device Letters* **2006**, 27, 737.

[40] Schroeder, R.; Ullrich, B. *Appl. Phys. Lett*. **2002**, 81, 556.

[41] Sui, G.; Orbulescu, J.; Mabrouki, M.; Micic, M.; LeBlanc, R. M.; Liu, S.; Cormier, R. A.; Gregg, B. A. *J. Phys. Chem. B* **2002**, 106, 9335.

[42] Sui, G.; Orbulescu, J.; Mabrouki, M.; Leblanc, R. M.; Liu, S.; Gregg, B. A. *Chem. Phys. Chem*. **2002**, 12, 1041.

[43] Cormier, R. A.; Gregg, B. A. *Chem. Mater*. **1998**, 10, 1309.

[44] An, Z.; Yu, J.; Jones, S. C.; Barlow, S.; Yoo, S.; Domercq, B.; Prins, P.; Siebbeles, L. D. A.; Kippelen, B.; Marder, S. R. *Adv. Mater*. **2005**, 17, 2580.

[45] Struijk, C. W.; Sieval, A. B.; Dakhorst, J. E. J.; Dijk, M. V.; Kimkes, P.; Koehorst, B. M.; Donker, H.; Schaafsma, T. J.; Picken, S. J.; Craats, A. M.; Warman, J. M.; Zuilhof, H.; Sudhölter, E. J. R. *J. Am. Chem. Soc.* **2000**, 122, 11057.

[46] Tam-Chang, S. W.; Iverson, I. K.; Helbley, J. *Langmuir* **2004**, 20, 342.

[47] Herrikhuyzen, J.; Syamakuri, A.; Schennig, A. P. H. J., Meijer, E. W. *J. Am. Chem. Soc.* **2004**, 126, 10021.

[48] Duff, J.; Hor, A. M.; Melnyk, A. R.; Teney, D.; *SPIE,* **1990**, 1253, 183.

[49] Nolde, F.; Wojciech, P.; Müller, S.; Kohl, C.; Müllen, K. *Chem. Mater*. **2006**, 18, 3715.

[50] Balakrishnan, K.; Datar, A.; Naddo, T.; Huang, J.; Oitker, R.; Yen, M.; Zhao, J.; Zang, L. *J. Am. Chem. Soc.* **2006**, 128, 7390.

[51] Klebe, G.; Graser, F.; Haedicke, E.; Berndt, J. *Acta Crystallogr. Sect. B: Struct. Sci.* **1989**, B45, 69.

[52] Kazmaier, P. M.; Hoffmann, R. *J. Am. Chem. Soc*. **1994**, 217, 507.

[53] Quante, H.; Geerts, Y.; Müllen, K. *Chem. Mater*. **1997**, 9, 495.

[54] Qu, J.; Kohl, C.; Pottek, M.; Müllen, K. *Angew. Chem. Int. Ed.* **2004**, 43, 1528.

[55] Tang, T.; Qu, J.; Müllen, K.; Webber, S. E. *Langmuir*, **2006**, 22, 7610.

[56] Tang, T.; Qu, J.; Müllen, K.; Webber, S. E. *Langmuir* **2006**, 22, 26.

[57] Iverson, I.; Tam-Chang, S. *J. Am. Chem. Soc*. **1999**, 121, 5801.

[58] Iverson, I. K.; Casey, S. M.; Soo, W.; Tam-Chang, S. *Langmuir* **2002**, 18, 3510.

[59] Marcon, R. O.; Santos, J. G.; Figueiredo, K. M.; Brochsztain, S. *Langmuir* **2006**, 22, 1680.

[60] Martinson, A. B. F.; Massari, A. M.; Lee, S. J.; Gurney, R. W.; Splan, K. E.; Hupp, J. T.; Nguyen, S. T. *J. of The Electrochem. Soc.* **2006**, 153, A527.

[61] Hosoi, Y.; Tsunami, D.; Ishii, H.; Furukawa, Y. *Chem. Phys. Lett*. **2007**, 436, 139.

[62] Podsaidlo, P.; Paternel, S.; Rouillard, J.-M.; Zhang, Z.; Lee, J.; Lee, J.-W.; Gulari, E.; Kotov, N.A. *Langmuir*, **2005**, 21, 11915.

[63] Chen, D.; Wang, G.; Lu, W.; Zhang, H.; Li, J. *Electrochemistry Communications* **2007**, 9, 2151.

[64] Kumar, S. K.; Hong, J. D.; Lim, C. H.; Park, S.Y. *Macromolecules* **2006**, 30, 3217.

[65] Man, K. Y. K.; Wong, H. L.; Chan, W. K.; Djurišić, A. B.; Beach, E.; Rozeveld, S. *Langmuir* **2006**, 22, 3368.

[66] Chiarelli, P. A.; Johal, M. S.; Holmes, D. J.; Casson, J. L.; Robinson, J. M.; Wang, H.-L. *Langmuir* **2002**, 18, 168.

[67] Everett, T. A.; Twite, A. A.; Xie, A.; Battina, S. K.; Hua, D. H.; Higgins, D. A. *Chem. Mater*. **2006**, 18, 5937.

[68] Song, Y. I.; Kim, G. Y.; Choi, H. K.; Jeong, H. J.; Kim, K. K.; Yang, C.-M.; Lim, S. C.; An, K. H.; Jung, T.; Lee, Y. H. *Chem. Vap. Deposition* **2006**, 12, 375.

[69] Meng, H.; Sun, F.; Goldfinger, M. B.; Gao, F.; Londono, D. J.; Marshal, W. J.; Blackman, G. S.; Dobbs, K. D.; Keys, D. E. *J. Am. Chem. Soc.* **2006**, 128, 9304.

[70] Datar, A.; Oitker, R.; Zang, L. *Chem. Comm*. **2006**, 1649.

[71] Datar, A.; Balakrishman, K.; Yang, X.; Zuo, X.; Huang, J.; Oitker, R.; Yen, M.; Zhao, J.; Tiede, D. M.; Zang, L. *J. Phys. Chem. B* **2006**, 110, 12327.

[72] Farhat, T.; Yassin, G.; Dubas, S.T.; Schlennoff, J. B. *Langmuir* **1999**, 15, 6621.

[73] Wu, G.; Su, Z. *Chem. Mater*. **2006**, 18, 3726.

[74] Zapotoczny, S.; Golonka, M.; Nowakowska, M. *Macro. Rapid Commun*. **2005**, 26, 1049.

[75] Xie, A.; Bei, L.; Hall, J E.; Barron, S. L.; Higgins, D. A. *Langmuir* **2005**, 21, 4139.

[76] Gundlach, D. J.; Lin, Y. Y.; Jackson, T. N.; Nelson, S. F.; Schlom, D. G. *Electron Device Lett*. **1997**, 18, 87.

[77] Vusser, S. D.; Steudel, S.; Myny, K.; Genoe, J.; Heremans, P. *Appl. Phys. Lett*. **2006**, 88, 103501.

[78] Gregg, B. A. *J. Phys. Chem*. **1996**, 100, 852.

[79] Gregg, B. A.; Sprague, J.; Peterson, M. W. *J. Phys. Chem. B* **1997**, 101, 5362.

[80] Adams, D. M.; Kerimo, J.; Olson, E. J. C.; Zaban, A.; Gregg, B. A.; Barbara, P. F. *J. Am. Chem. Soc*. **1997**, 119, 10608.

[81] Zakrevskyy, Y.; Faul, C. F. L.; Guan, Y.; Stumpe, J. *Adv. Funct. Mater.* **2004**, 14, 835.

CHAPTER 2 - Experimental Considerations

2.1. Introduction:

This chapter describes the experimental aspects of the research performed for this thesis. First, the syntheses of the various water-soluble perylene diimides (PDIs) employed are covered. Next, the preparation of polyelectrolyte (PE) and PDI solutions is covered. A discussion of the layer-by-layer (LBL) electrostatic-self-assembly (ESA) methods used to prepare the PDI•PE composite films is then given. Next, characterization of the samples by UV-vis spectroscopy, dichroism studies, and atomic force microscopy (AFM) is described in detail. Finally, the statistical analyses used to assess fiber size and alignments are presented.

2.2. Synthesis of Starting Materials:

The PDIs used for PDI•PE composite preparation were synthesized using modifications of other reported procedures.[1,2,3,4,5,6] The structures of the PDIs employed are shown in figure 1. The syntheses of these compounds involve a condensation reaction with the appropriate primary amine precursor.

2.2.A. Synthesis of sodium bis (sulfonatopropyl) perylene diimide ($PDISO_3^{2-}$):

A paper authored by Ye has previously reported the synthesis of this compound; the entire synthesis of this compound will be described here.[1] The reactants needed for the synthesis of $PDISO_3^{2-}$ were the following: perylene-3,4,9,10-tetracarboxylic dianhydride (PTCDA), zinc acetate(a catalyst), and 3-aminopropane sulfonic acid. All compounds were used as received. The solvents employed were pyridine, hydrochloric acid, ethyl acetate, hexane, isopropanol, and ethyl ether. A single pot procedure was used in this synthesis.

A 500 mL round bottom flask was used, to which 472.9 mg (1.205 mmol) PTCDA, 555.3 mg (3.986 mmol) 3-aminopropane sulfonic acid, and 274.2 mg (1.249 mmol) zinc acetate were added. Next, 250 mL of pyridine was used to dissolve the reactants, while stirring under nitrogen. This mixture was refluxed for 7 days. Upon cooling, the solution was filtered through a Buchner funnel. The solid was washed with a 3:1 ethyl acetate: hexane mixture, and subsequently dried in a vacuum oven for several hours at 80ºC.

The product was next dissolved in slightly basic water and insoluble solids were removed by centrifuging. The solution was then mixed with an equal portion of 2 M HCl. Next, the solution was placed in an ice bath for two hours to precipitate the product. Then the precipitate was subsequently centrifuged and the supernatant liquid was removed. The solid was collected on a fritted filter and a dark red in color. This product was rinsed with (1:1) cold ethyl ether and isopropanol. The product was dried in a vacuum oven overnight at 80 ºC. The final dry product had a mass of 357.3 mg (47% yield).

2.2.B. Synthesis bis (trimethylammonioethyl) perylene diimide diiodide ($PDIDI^{2+}$):

The compounds needed for the synthesis of $PDIDI^{2+}$ were the following: perylene-3,4,9,10-tetracarboxylic dianhydride (PTCDA), iodomethane (CH_3I), potassium carbonate (K_2CO_3) and N,N-dimethylethylenediamine (DMED). The compounds were purchased from Aldrich and used as received. The synthesis was carried out by modifications of procedures reported elsewhere.[2,3,4,5,6] The solvents employed were pyridine, chloroform, acetone, and ethyl ether. A single pot procedure was used for $PDIDI^{2+}$ synthesis.

First, 340.5 mg (0.868 mmol) PTCDA was added to a 250 mL round bottom flask, along with 490 mg (5.564 mmol) dimethylethylenediamine. 100 mL of pyridine was used to dissolve the reactants. The reaction was then refluxed for 2 days with vigorous stirring. The pyridine was subsequently removed by rotary evaporation in a fume hood. A 100 mL portion of aqueous 6% K_2CO_3 was then added to the crude solid product and refluxed for 20 minutes. The solution was filtered while hot through a fritted glass funnel, and the product was then rinsed with K_2CO_3 and cold acetone. The product was dried in a vacuum oven at 65ºC for several hours. The mass of dry product obtained was 429 mg (93% yield).

198.4 (0.410 mmol) mg of the dried product (prepared above) was dissolved in 100 mL chloroform in a 250 mL round bottom flask. 1.2 mL (19.3 mmol) CH_3I was then added to this solution, and the solution was subsequently refluxed for 14 hours. The flask was cooled and the alkylated product collected on a Buchner filter. The product was rinsed three times with ethyl ether and dried in the vacuum oven at 85˚C. The final mass of product collected was 297.3 mg (97% yield).

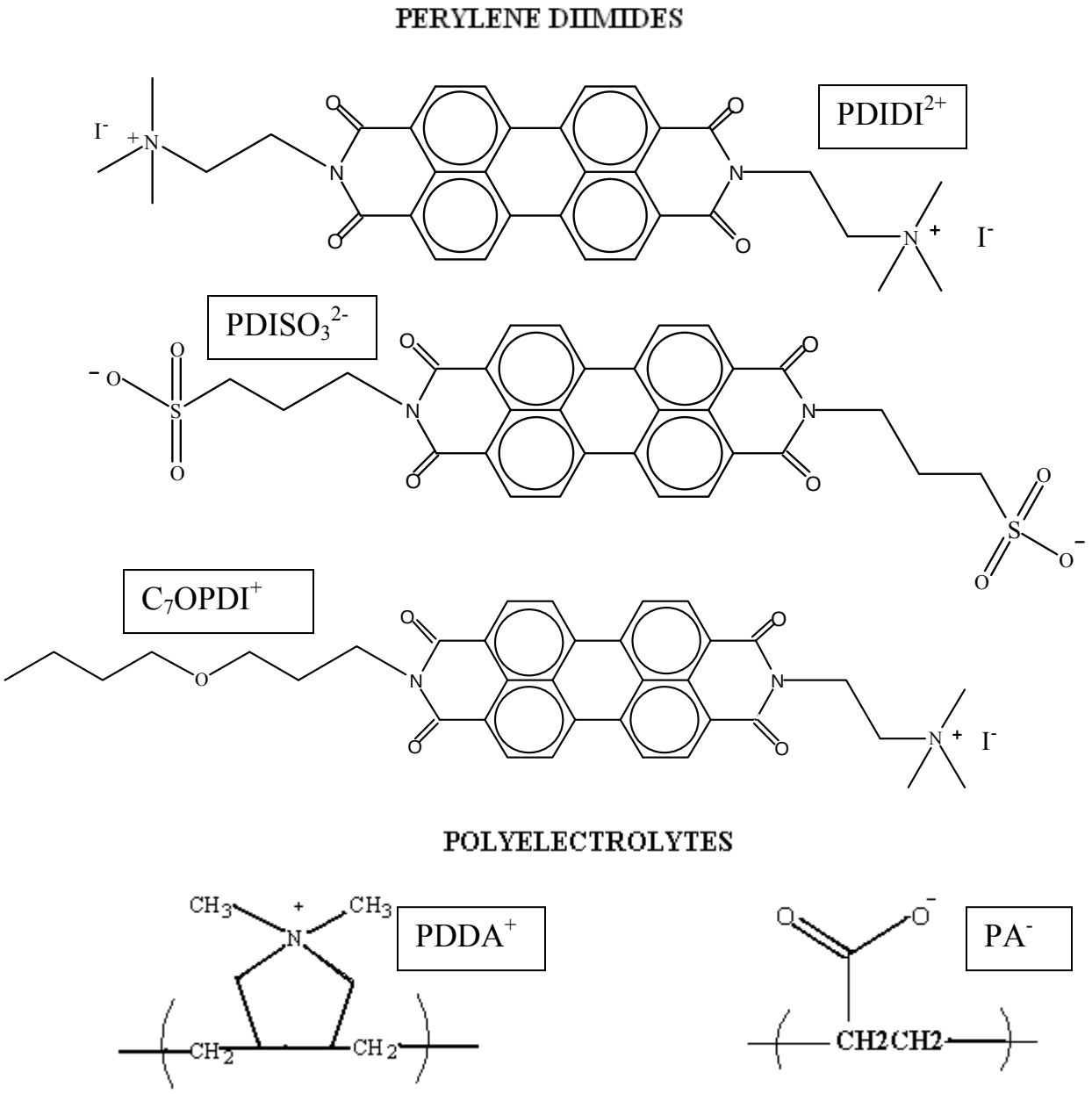

Figure 2.1. Structures of PDIs and PEs

Structures of the PDIs synthesized for use in LBL electrostatic self-assembly. The structures of the two counter polyelectrolytes (PEs) are also shown.

2.2.C. Synthesis of N-(butoxypropyl)-N'-(2-(N,N,N-trimethylammonio)ethyl) perylene-3,4,9,10-tetracarboxylic diimide iodide (C_7OPDI^+):

The compounds needed to prepare the C_7OPDI^+ were the following: perylene-3,4,9,10-tetracarboxylic dianhydride (PTCDA), N,N-dimethylethylenediamine (DMED), iodomethane (CH_3I), and 3-butoxyproplyamine (BPA). These compounds were obtained from Aldrich and used as received. The synthesis was based on modifications to procedures reported elsewhere.[2,3,4,5,6] The solvents employed were pyridine, ethanol, triethylamine and chloroform. A single pot procedure was used for preparation of the C_7OPDI.

A 25 mL round bottom flask had 0.61 (1.55 mmoles) g PTCDA, 0.45 g (3.41 mmoles) BPA, and 0.13 g (1.51 mmoles) DMED added to it. 15 mL pyridine was then added to the round bottom flask to dissolve the reactants. The solution was then refluxed under nitrogen for 17 h, with vigorous stirring. The flask was then allowed to cool and was subsequently rotary-evaporated to remove the pyridine and residual DMED. The solid product was collected on a filter using four portions of cold ethanol. The solid was then dried for 1 h at 70°C under vacuum. For purification 0.25 g of crude product was dissolved in a mobile phase of 10:1:0.1 ($CHCl_3$:EtOH:Et_3N). A 15 inch column was used for the separation. Pure product was obtained here by dividing the dry crude product into three portions, with each chromatographed separately. The C_7OPDI product was again obtained as the second band emerging from the column. The impure and pure fractions were saved.

The impure and pure C_7OPDI fractions were next dissolved in a mobile phase of (20:1:0.2) $CHCl_3$:EtOH:Et_3N. A 15 inch column was again used. Pure C_7OPDI was again obtained as the second band emerging from the column. The C_7OPDI fractions were rotary-evaporated down and collected on a filter using four portions of cold ethanol. The solid was vacuum dried at 50°C for 1 h. A total of 60 mg of the asymmetric C_7OPDI product was collected in the high purity. The NMR results proved the purity of the product. ^1H NMR (400 MHz, $CDCl_3$) 8.4 (m, 8 H perylene), 4.36 (m, 4H, CH_2N), 3.60 (t, 2H, CH_2O), 3.43 (t, 2H, CH_2O), 2.72 (t, 2H, CH_2N), 2.42 (s, 6H, $(CH_3)_2N$), 2.08 (t, 2H,CH_2), 1.5 (t, 2H, CH_2), 1.35 (t, 2H, CH_2), 0.85 (t, 3H, CH_3).

Synthesis of the asymmetric C_7OPDI^+ was then carried out using pure C_7OPDI. All 60 mg (0.1 mmol) of the high purity C_7OPDI was dissolved in 50 mLs $CHCl_3$ by stirring and heating. The solution was filtered to remove insoluble solids. To this solution was added 200

μL (3.2 mmol) Iodomethane. The solution was refluxed for 6 h. The reaction mixture was then cooled overnight. A rotary-evaporator was then used to concentrate the reaction mixture. The remaining solution had 2 parts ethanol added to it, and was then centrifuged, with the supernatant removed afterwards. The remaining solid was rinsed with diethyl-ether twice. The solution was centrifuged again with subsequent removal of the supernatant. The remaining solution was transferred to a small flask for removal of the diethyl ether by rotary-evaporation. There was 46 mg (64% yield) of dry C_7OPDI^+ product collected.

2.3. Preparation of PDI and Polyelectrolyte Solutions:

Poly(diallyldimethylammonium chloride) ($PDDA^+$) 20% by wt. in water and poly(acrylic acid) (PA^-) were purchased from Aldrich and used as received. The $PDDA^+$ solution was made by transferring 0.233 mL (3mM monomer) stock to a 100 mL volumetric flask. This was diluted to volume with 0.1 M phosphate buffer (pH 7). A 0.1 M phosphate buffer (pH 7) solution was used to fix the ionic strength and pH of the PE solution. Higher ionic strength makes the PE deposit faster by causing more and longer aggregates to form in solution. PA^- solutions were prepared by weighing 28.8 mg of PA^- into a 100 mL volumetric flask. The solution was dissolved in a 100 mL 0.1 M phosphate buffer solution (pH 7) in a volumetric flask to give a final concentration of 3mM monomer PA^-. The structures of both PEs can be seen in figure 1.

The PDI solutions were prepared using the following procedures. $PDISO_3^{2-}$ solutions were prepared by dissolving 15.7 mg $PDISO_3^{2-}$ in 100 mL of high purity water. $PDISO_3^{2-}$ solutions required stirring and heating for complete dissolution of the solid. The final concentration of the $PDISO_3^{2-}$ was 245 μM. The $PDIDI^{2+}$ solution was made by dissolving 9.7 mg in 1:1 methanol and high purity water, with heating and stirring. The methanol was subsequently boiled off after the entire solid had dissolved. A second portion of water was added and the solution was evaporated to half the volume by boiling again. Finally, the solution was diluted to volume (50 mL) using high purity 18 MΩ•cm water. The final $PDIDI^{2+}$ concentration was 245 μM. The C_7OPDI^+ solution was made by dissolving 18 mg of solid in 60 mL of methanol, with stirring and heating. The methanol was boiled down to half of the original volume after the solid dissolved. Next, an equivalent amount of high purity water was added and the volume was again reduced to half by boiling. This procedure was then repeated a second

time to ensure removal of all methanol. Finally, the solution was transferred to a 100 mL volumetric flask and diluted to volume with high purity water to yield a final concentration of 251 μM.

10 μM PDI solutions were made for obtaining the absorbance spectrum and fraction aggregated of the PDI in precursor solutions. The solutions were prepared by transferring approximately 1.020 mL of stock PDI solution to a 2, 25 mL volumetric flask. Then the two flasks were diluted to volume with either methanol or high purity 18 MΩ•cm water. The solutions then immediately had their absorbance and emission spectra taken.

2.4. Instrumentation:

The instrumentation used for the experiments described in this thesis can be broken into three categories. The first is instrumentation needed for sample preparation and deposition. The second is for the bulk sample characterization. The final section will look at the high resolution imaging experiments.

2.4.A. Sample Preparation and Deposition:

All samples used in this thesis were prepared on glass cover slips (Fisher Premium). A Harrick Plasma Cleaner (PDC-326) was used to clean the cover slips. Each cover slip was treated for at least 5 minutes in the plasma cleaner prior to use. A homemade computer-controlled dip coater was used to deposit the PDIs and PEs (See figure 2) on the cover slips. A Lab View program (written in house) ran the dip coater.

2.4.B. Bulk Sample Characterization:

A HP 8453 UV-vis spectrometer was used for recording the absorption spectra for the solution studies and all the thin films. A home built slide holder was used to reproducibly position the glass cover slips in the optical path. This sample holder was also designed to hold a sheet polarizer in front of the sample for dichroism studies.

A Fluoromax 2 fluorometer was used to determine the fluorescence emission intensity for the 10 μM PDI solutions. In all spectra, the excitation wavelength was 488 nm, scan range was 500-700 nm, data was acquired at 1 nm increments, a 1 second integration time was used, and the slit widths were 1 nm. This allowed for the determination of the fraction aggregated. The fraction aggregated was found by equation 1.

$$\text{Fraction Aggregated} = \frac{I_{Max(methanol)} - I_{Max(water)}}{I_{Max(methanol)}}$$

Equation 2.1. Fraction Aggregated

In equation 2.1, $I_{max(methanol)}$ is the fluorescence intensity maximum for the PDI in the methanol. $I_{max(H2O)}$ is the fluorescence intensity maximum for PDI in dissolved in water.

2.4.C. High Resolution Microscopic Sample Preparation and Imaging:

AFM specimen discs (pucks) 15 mm in diameter were obtained from Ted Pella and were used in the AFM studies. The pucks are round magnetic disks to which samples were affixed using a thin layer of an elastomeric polymer. The elastomeric polymer used was a two-part commercial silicone product (SylGard 184). The Elastomer Base and Elastomer curing agent were mixed in a 10:1 ratio by weight, as recommended by the manufacturer. The AFM puck was placed on a Specialty Coating System P-6000 spin coater and held there with double sided tape. Two drops of the mixture were placed on the puck, and the puck then was spun at 2000 rpm for 2 minutes. The film was then allowed to dry overnight in a drying cabinet. The puck was then ready for use.

The sample had to be cut down to size to fit in the AFM before analysis could be done. For this purpose, a square was cut out of the middle of each sample and was placed onto the puck. The middle of the sample was chosen as the best representation of the entire film. This region of the sample was judged to have minimal effects from surface tension that the sides would experience. The bottom of the sample was not chosen because the bottom was exposed to the solution longer than other parts of the sample. The top of the sample was also deemed unacceptable because of the air water interface where visibly more PDI was deposited. The size of the cut glass cover slip was large enough to fit on the puck with none of the sample hanging over the puck edge. Also, the size was large enough to minimize the chances of finding cutting debris in the region imaged.

Digital Instruments MultiMode AFM operating in tapping mode analyzed the samples. The AFM was operated in height mode. Typically, the AFM scans were of 10 x 10 μm or 25 x 25 μm regions of the sample. Three images were taken at different regions on each film. Each image was comprised of 512 x 512 pixels. In all experiments, the AFM raster scan rate was set

between 10 μm/sec and 12.5 μm/sec, yielding a line scan frequency between 0.50 Hz and 0.25 Hz.

2.5. Thin Film Deposition:

The thin films were made on plasma cleaned cover slips (see above). Clean cover slips were stored in a covered Petri dish until use. All cover slips were used within a day after being plasma cleaned. All the films investigated in this thesis were prepared by layer-by-layer (LBL) electrostatic-self-assembly (ESA) using the dip coater shown in figure 2. Film preparation involved repeated dipping of the glass substrate into four solutions. The cover slips were first lowered into cationic precursor solution. After removal from this solution, the weakly bound material was removed by dipping the slide into a rinse beaker. The substrate was then dipped into the anionic precursor solution and again rinsed to remove unbound material. The time spent in each of the four beakers was 60, 30, 60, and 30 seconds, respectively. In the early experiments the substrate was raised and lowered in the solutions at a rate of 1.8 mm/sec. Later, the withdrawal rate was varied to study the effect of the dip rate on film morphology. The films made from the different PDIs and PEs were prepared with 5, 10, 15, 20, 25, and 30 bilayers. In this thesis, the term "bilayers" refers to deposition of both the cationic and anionic precursor layer on the substrate. The coated cover slip was allowed to air dry after the desired number of bilayers had been deposited. The cover slips were stored in a covered petri dish until analysis.

2.6. Analysis of Thin Films:

Bulk analysis of the samples was carried out by recording their UV-vis absorption spectra. A sheet polarizer was used for the dichroism studies and was inserted in the beam path, prior to the sample. Analysis of the nanoscale properties of the films was performed by Atomic Force Microscopy (AFM). Various statistical analysis programs were used to determine fiber widths and alignment characteristics from the UV-vis and AFM data.

2.6.A. UV-vis Absorption Spectroscopy:

The bulk spectroscopic properties of the PDI•PE films were analyzed by UV-vis absorption spectroscopy. The UV-vis allowed for the absorption spectra of the films to be recorded as a function of the amount of material deposited. The absorbance of one of the PDI•PE films is shown in figure 3.

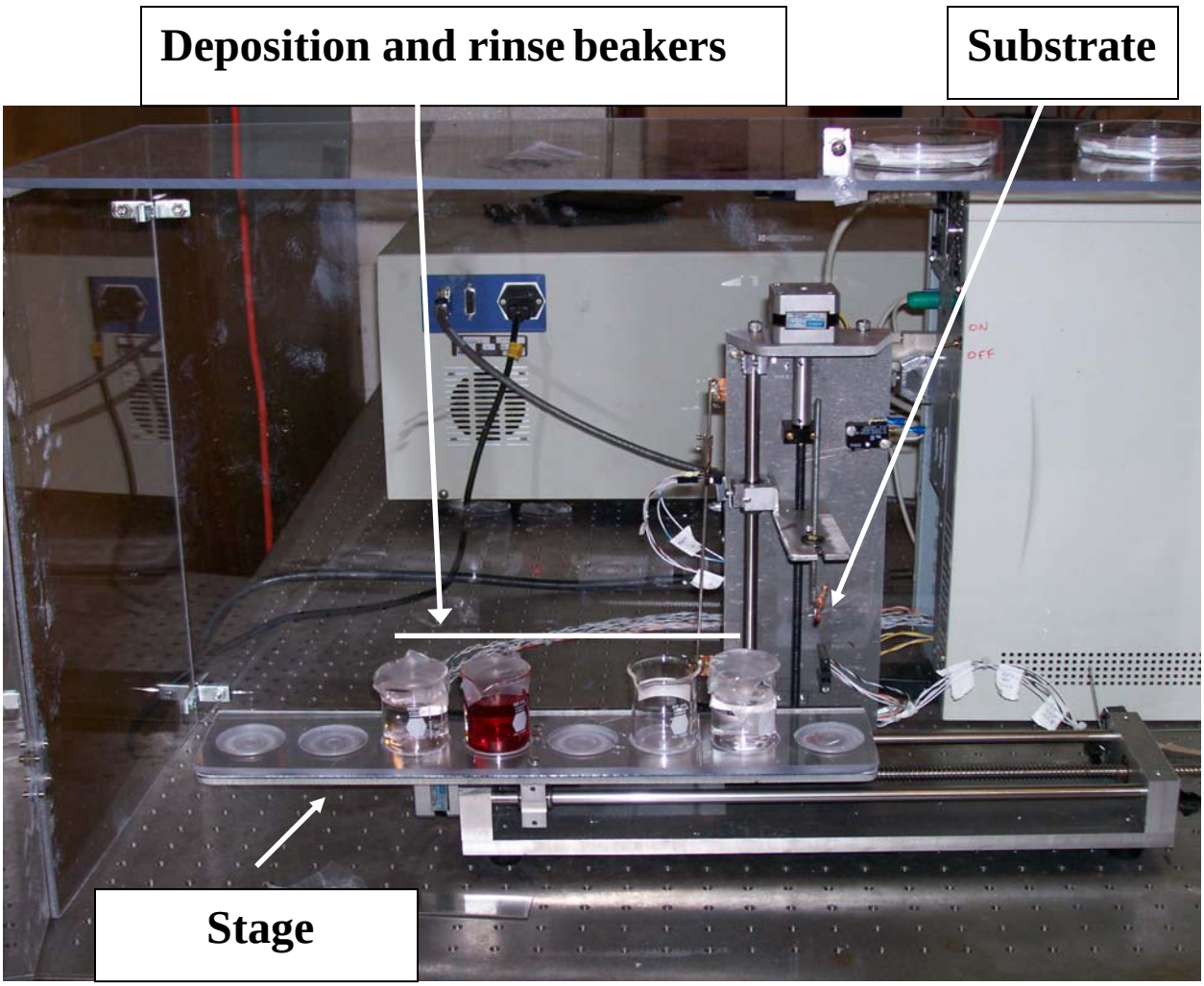

Figure 2.2: Dip Coater

Computer controlled dip coater used in this thesis. An alligator clip was used to hold the substrate. The dip coater stage moves from left to right. The substrate insertion and withdrawal rate was set to 1.8 mm/sec. Each beaker contained approximately 40 mL of solution. All solutions were stored in a covered box to keep them in the dark until use.

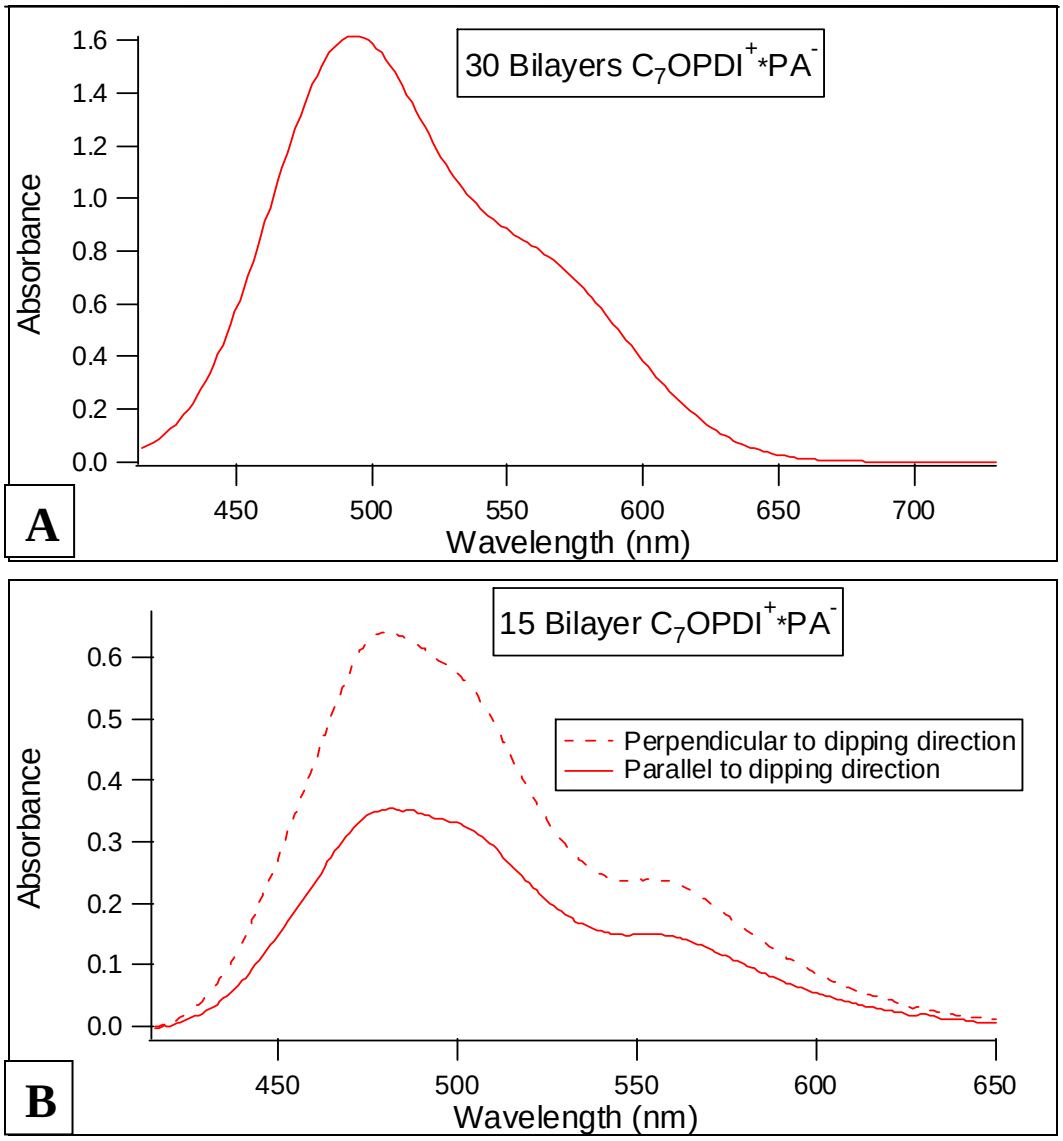

Figure 2.3. Absorbance Spectra

Example spectra of the thin films studied in this thesis. A) Corrected spectrum of a 30 bilayer sample prepared using 252μM C_7OPDI^+ and 3mM PA^- (in a 0.1 M phosphate buffer (pH 7)). B) Absorbance spectra for 15 bilayers of $C_7OPDI^+ \bullet PA^-$. The solutions used to prepare the film were 206 μM C_7OPDI^+ and 3mM PA^- (in a 0.1 M phosphate buffer (pH 7)). Spectra are shown for light polarized perpendicular and parallel to the dipping direction.

The samples were background corrected by use of a macro (written in house) for Igor graphing software. Background correction was made necessary, because of light scattering by the sample, which leads to a sloped baseline. After the samples were background corrected, the peak absorbance value was found, along with peak wavelength. The peak wavelength varied with the number of bilayers. The peak maximum for the three types of composite films at 30 bilayers was for the 490 nm, 504 nm, and 498 nm for C_7OPDI^{+}•PA^{-}, $PDIDI^{2+}$•PA^{-}, and $PDISO_3^{2-}$ •$PDDA^{+}$ respectively. The peak maximum wavelength varied by 10 nm for all samples studied. After the absorbance for each sample was determined, the absorbance as a function of bilayer number was plotted. This data is presented in chapter 3.

A Polarizer was used for measurements of film dichroism and hence, bulk fiber alignment in the composites. The sample was first placed in the sample holder, so the dipping direction was parallel to the polarization of the incident light. After this spectrum was taken, the sample was rotated 90º to record the spectrum for light polarized perpendicular to the dipping direction. A difference in peak absorbance for these two polarizations was usually observed, see figure 3(B). Equation 2 was used to find the dichroism of the bulk composites from the absorbance values. The dichroism values obtained were plotted as a function of bilayer number for the composite films in fiber alignment studies.

$$D = \frac{(A_{\parallel} - A_{\perp})}{(A_{\parallel} + A_{\perp})}$$

Equation 2.2. Dichroism

In equation 2.2, D is the dichroism, $A_{\parallel}$ is the absorbance for light polarized parallel to the dipping direction, and $A_{\perp}$ is the absorbance for light perpendicular to the dipping direction.

2.6.B. Studies of Sample Morphology:

2.6.B.1. Fiber Dimensions:

Fiber dimensions were determined as a function of bilayer number. Figure 4 shows representative images of the PDI•PE samples used in these studies. Fiber dimensions were obtained by autocorrelating the images using a Lab View program (written in house).[7,8,9] Quantitative data on nanofiber size was obtained as the result of the analysis. Equation 3 was used in the calculation. The points of interest in the autocorrelated data are only the center 5%. To find the average fiber widths, an exponential equation was used to fit the data, as shown in

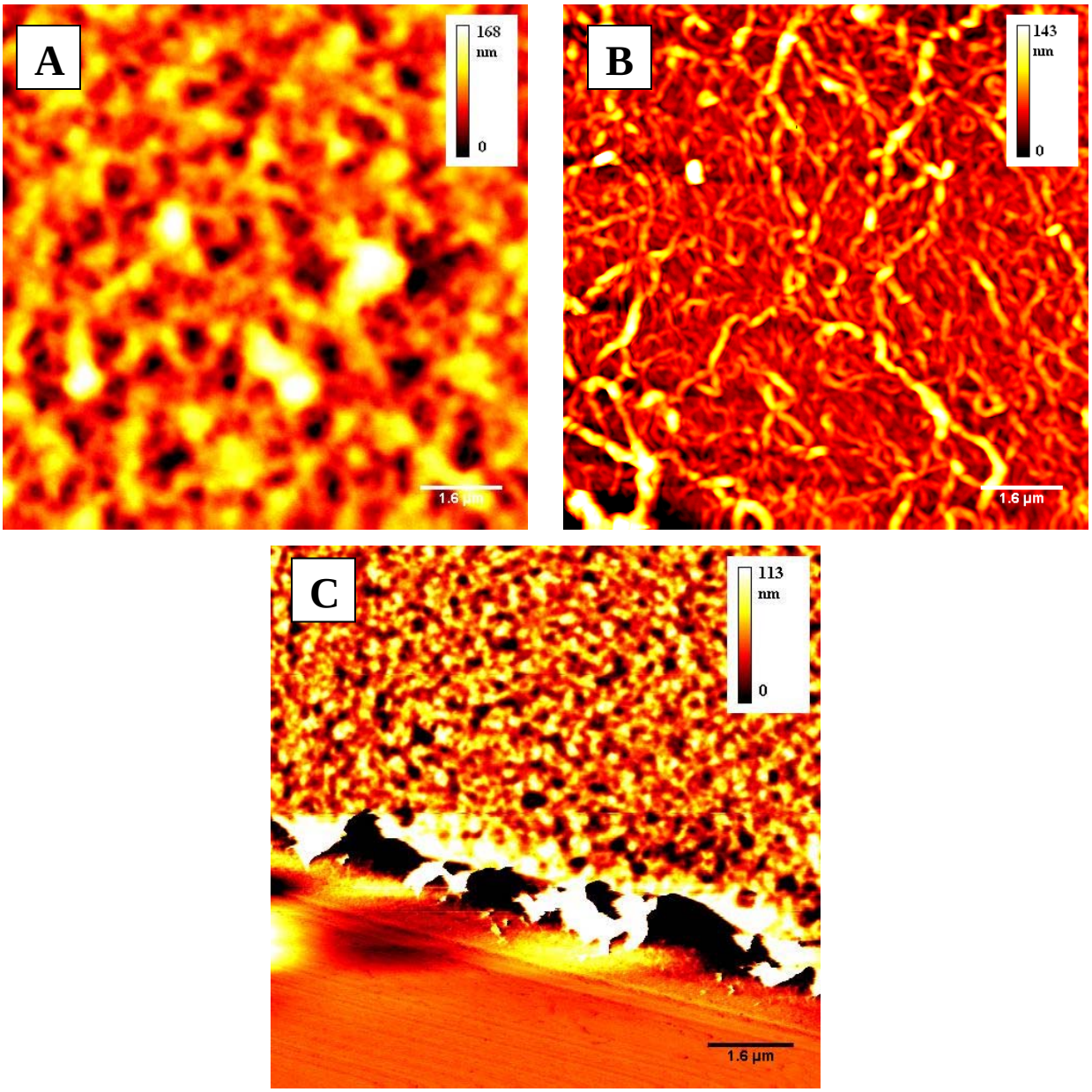

Figure 2.4. AFM Images

A) This is a representative AFM image 10 x 10 µm region showing no apparent fiber alignment. The sample was comprised of 20 bilayers of $PDISO_3^{2-}$•$PDDA^+$. B) Representative AFM image of 10 x 10 µm region showing the nanofiber alignment for a 20 bilayer C_7OPDI^+•PA^- film. C) Representative image of a 25 x 25 µm region containing a scratch. Such images were used for thickness measurements. This sample is comprised of 10 bilayers of $PDIDI^{2+}$•PA^- composite.

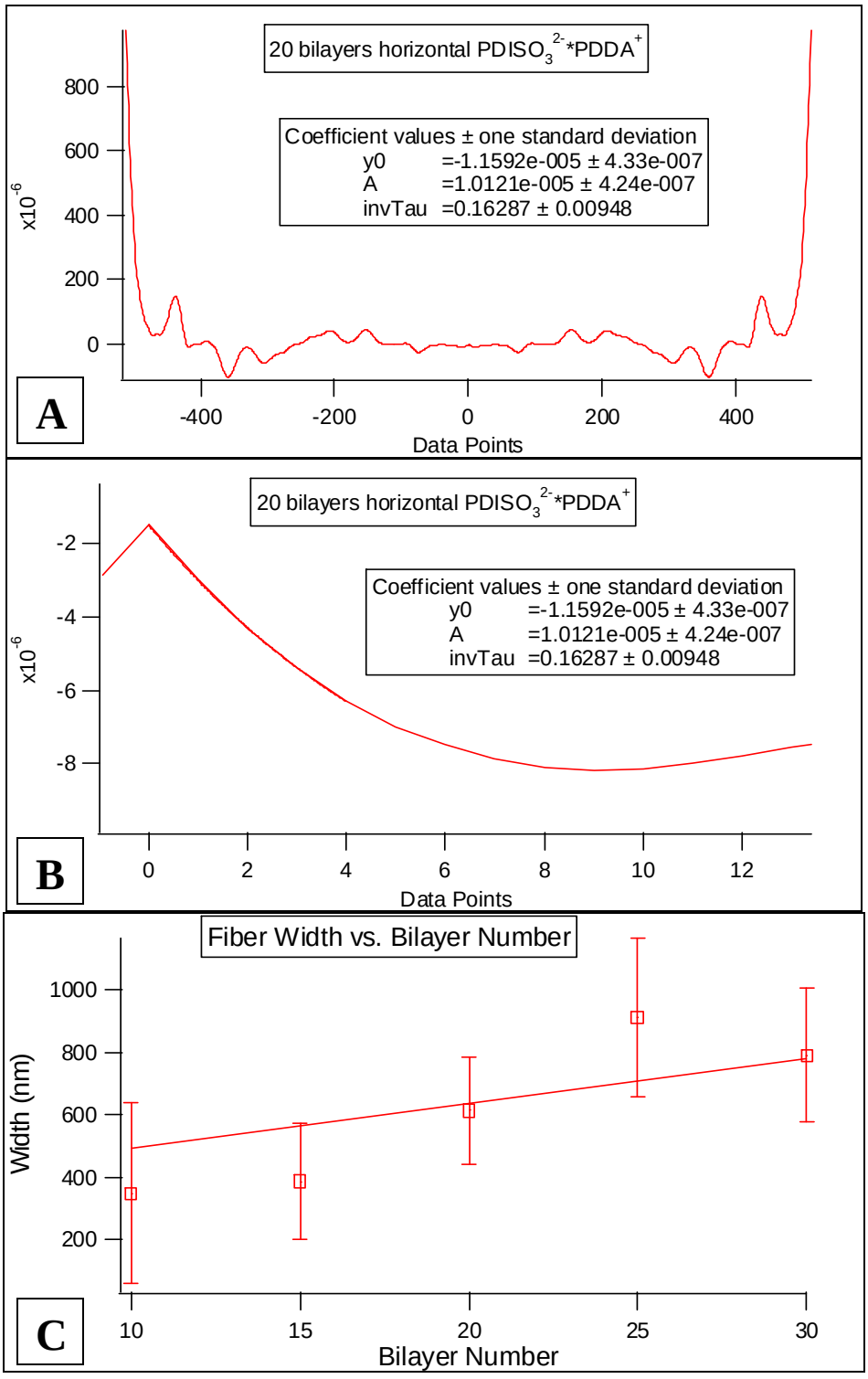

Figure 2.5. Autocorrelation Data Points for Fiber Width

(A) Autocorrelation function obtained from a represent AFM image. (B) Center data points fitted to an exponential equation. (C) Average Fiber width vs. bilayer number for the $PDISO_3^{2-}$ •$PDDA^+$ composites.

figure 5(A). The inverse of the exponential decay constant in each direction was taken as the width in that direction. The width was found in both the vertical and the horizontal directions; the two values were averaged together. The width was plotted as a function of bilayer number, as shown figure 5(C).

$$C(\xi,\varphi) = \frac{\langle h(x+\xi, y+\varphi)h(x,y)\rangle}{\langle h(x,y)\rangle^2}$$

Equation 2.3 Autocorrelation Equation

In equation 3, h(x,y) represents the topographic height at points x,y in the image. C(ξ,φ) is the autocorrelation function obtained. The brackets indicate a spatial average is taken during the calculation.

2.6.B.2. Determination of Film Thickness:

The film thickness was also determined by AFM. This was done by using razor blade to remove the PDI•PE composite down to the glass substrate surface. The vicinity of the scratch was then imaged with the AFM. The part that did contain the scratch then was flattened to properly determine the film thickness. A Lab View Program (written in house) was used to determine the average film height from three different regions in each image. Film thickness as a function of bilayer number was plotted for all the composites.

2.6.B.3. Fiber Alignment:

Samples showing dichroism in the bulk were further analyzed by AFM. These experiments were used to characterize the film morphology and fiber order on the nanometer scale. An example of a sample showing alignment is given in figure 6(A). Images of these samples were processed using a Lab View Program (written in house) to determine the amount of alignment present. The program describing the calculations for the orientation of the fibers was similar to one described by Elbishinger.[10] How the program works will briefly be described here. The first step involved finding the derivative in both the vertical(y) and horizontal direction(x). Next, the second derivative for the image (I) was determined in four directions (xx, xy, yx, and yy). This gives a Hessian matrix as defined in equation 4.[11] The eigenvectors and eigenvalues of the Hessian were then determined. The positive eigenvalues obtained gave the ridges image. This image more clearly shows the fibers, see figure 6(B), and defines the highest

points along each fiber. The thresholded ridges image was then used as a "mask" to determine fiber orientation from the eigenvector data. The population of fibers at every angle was summed. This was plotted in a graph with the population as a function of angle of orientation.

$$\left(\nabla_u^2 I\right) = \begin{pmatrix} I_{xx} & I_{xy} \\ I_{yx} & I_{yy} \end{pmatrix}$$

Equation 2.4 Hessian Equation

In equation 4, the Hessian is an equation described as a gradient of a gradient vector field. Here I is the image data and ∇_u^2 represent the second derivative of the image along u.

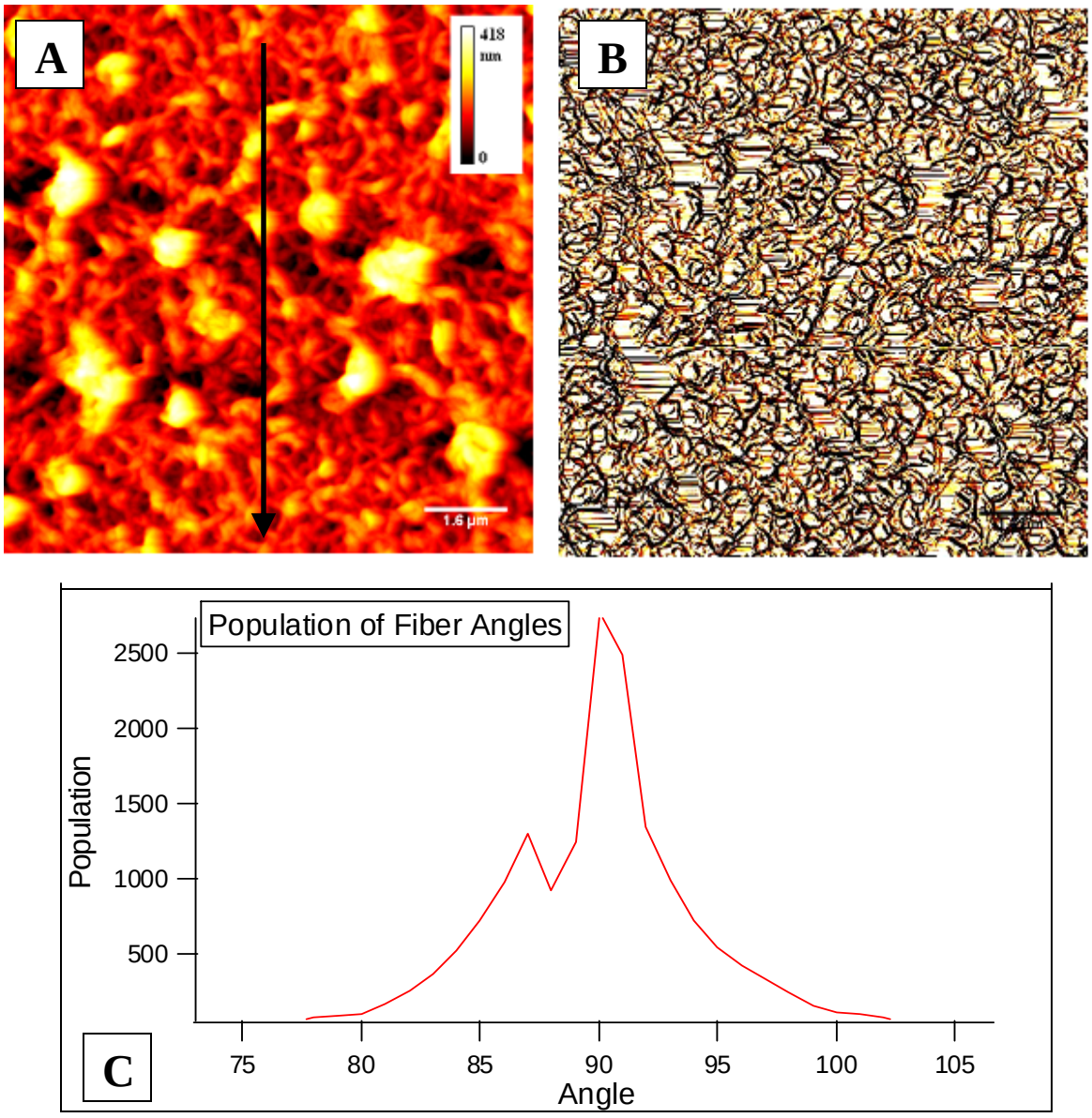

Figure 2.6(A) 20 bilayer composite, (B) Ridges Image, and (C) Histogram of alignment

(A) A 10 x 10 µm AFM image of a 20 bilayer composite displaying fiber alignment. The direction of the deposition is shown by the arrow. (B) The same image showing the ridges image generated from the analysis program. (C) Histogram generated from the fiber analysis software. This histogram displays the population of fiber angles for this composite. This image dictates that there is a greater occurrence of fibers aligned parallel to flow direction.

References

[1] Ye, F.; Higgins, D. A.; Collinson, M. M. *J. Phys. Chem. C* **2007**, 111, 6772.

[2] Guan, Y.; Zakrevskyy, Y.; Stumpe, J.; Antonietti, M.; Faul, C. F. J.; *Chem. Commun*. **2003**, 106, 1307.

[3] Iverson, K. I.; Tam-Chang, S. *J. Am. Chem. Soc*. **1999**,121, 5801.

[4] Iverson, K. I.; Casey, S. M.; Wonewoo, S.; Tam-Chang, S. *Langmuir* **2002**, 18, 3510.

[5] Cormier, R. A.; Gregg, B. A. *Chem. Mater*. **1998**, 10,1309.

[6] Liu, S.; Sui, G.; Cormier, R. A.; Leblanc, R. M.; Gregg, B. A. *J. Phys. Chem. B* **2002**, 106, 1307.

[7] Schlettwein, D. Back, A.; Schilling, B.; Fritz, T.; Armstrong, N. R. *Chem. Mater.* **1998**, 10, 601.

[8] Everett, T. A.; Twite, A. A.; Xie, A.; Battina, S. K.; Hua, D. H.; Higgins, D. A. *Chem. Mater*. **2006**, 18(25); 5937.

[9] Petersen, N. O.; Höddelius, P. L.; Wiseman, P. W.; Seger, O.; Magnusson, K. E. *Biophysical Journal* **1993**, 65, 1135.

[10] Elbischger, P. J.; Bishof, H.; Regitnig, P.; Holzapfel, G. A. *Pattern Anal. Applic*. **2004**, 7, 269.

[11] Gradshteyn, I. S.; Ryzhik, I. M. Tables of Integrals, Series, and Products, 6th edn. Academic Press, San Diego, California, Chapter 14, 314.

CHAPTER 3 - Towards Control of Perylene Diimide•Polyelectrolyte Composite Thin Film Growth and Morphology

3.1. Introduction:

Several different moieties of perylene diimides (PDIs) were investigated for their thin film growth and morphology forming properties. PDIs happen to be a class of n-type organic semiconducting materials and are one of the few which are air stable. PDIs were chosen as the molecular semiconductor to investigate because of potential uses demonstrated in previous experiments. Among these uses are electrochromic devices,[1] light emitting diodes,[2] light harvesting applications,[3] p-n junctions,[4,5] liquid crystal materials,[6] nanowires,[7,8] and organic field effect transistors.[9] The starting material, perylene-3,4,9,10-tetracarboxylic dianhydride (PTCDA) was tailored to be water-soluble, thus minimizing the use of environmentally unfriendly solvents. The resulting water-soluble compounds are sodium bis (sulfonatopropyl) perylene diimide ($PDISO_3^{2-}$), bis (trimethylammonioethyl) perylene diimide diiodide ($PDIDI^{2+}$), and N-(butoxypropyl)-N'-(2-(N,N,N-trimethylammonio)ethyl) perylene-3,4,9,10-tetracarboxylic diimide iodide (C_7OPDI^{+}). What is of particular interest is how nanofeatures form on the surface and grow when these PDIs are deposited in composite films.

The PDIs were investigated using a dip coater to create thin films of PDIs and polyelectrolytes (PEs). The dip coating method involves electrostatic-self-assembly (ESA) of the PDIs and PEs to form thin films. By using oppositely charged PDIs and PEs, the film's growth can be controlled in a layer-by-layer (LBL) process.[10] LBL methods for film growth have been used with a wide variety of molecules including carbon nanotubes with charged ionic polyelectrolytes adsorbed onto nanotubes.[11,12,13] LBL methods are predominately solution based. Similar procedures reported in the literature show water-soluble PDIs form thin films and in layers.[18,19] In this thesis work, only pseudo layers will form. The pseudo layers stem from the tendency for fiber formation instead of layers with some PDI compounds.

The pseudo layers are examined to see how these effect film formation and the features formed. In the process observed here, a finite amount of PDI aggregates attach to the surface in each deposition cycle. When the substrate is immersed in the anionic solution some of the anionic compound adsorbs where the surface charge has been reversed by deposition of the cationic compound. These small areas where the charged molecules have deposited, then act as sites where the fiber nucleation extends out. This extension of fiber growth occurs due to electrostatic attraction of the oppositely charged molecules. Also, π-π stacking of the aggregates together increases the fibers length. This group observed this process in earlier work.[14]

The investigations carried out here examined the effect three different water-soluble PDIs have on the thin film forming properties. The films were quantified by bulk absorbance measurements to determine how much the PDIs are present in the film. This technique works well, because the PEs possess no conjugation and no π bonds, thus they do not adsorb in the same spectral range as PDI. Special attention was paid to the fibers structure and width on the surface of the films. The effect of different PDI moieties on the fibers appearance was closely examined. This shows how the various surface fibers growth affects the overall thickness of the composite films.

3.2. Experimental:

3.2. A. Synthesis of Starting Film Precursors:

The detailed procedure for the synthesis of the PDI starting materials of sodium bis (sulfonatopropyl) perylene diimide ($PDISO_3^{2-}$), bis (trimethylammonioethyl) perylene diimide diiodide ($PDIDI^{2+}$), and N-(butoxypropyl)-N'-(2-(N,N,N-trimethylammonio)ethyl)perylene-3,4,9,10-tetracarboxylic diimide iodide (C_7OPDI^{+}) can be found in 2.2.A., 2.2.B., and 2.2.C. of this thesis, respectively. The procedure for production of the precursor perylene diimides (PDIs) and polyelectrolyte (PEs) solutions can be found in chapter 2.3 of this thesis.

10 μM PDI solutions were prepared for determination of their bulk aggregation state. The preparation of 10 μM PDI solutions involved dilution of concentrated stock solutions. This was accomplished for the $PDISO_3^{2-}$ by transferring 1.012 mL of stock 245 μM solutions into 2, 25 mL volumetric flasks. One flask was diluted to volume with methanol. The second was diluted to volume with 18 MΩ•cm high purity water. This same procedure was repeated for the other two PDIs used in the study.

3.2.B. Thin Film Formation:

Thin films were deposited in an ESA-based LBL process using a linear dip coater described in chapter 2.4.C. of this thesis. The dip coater was enclosed in Plexiglas to keep any dust or other material from drifting into the precursor solutions. The precursors were deposited by alternating cationic and anionic solutions with rinse solutions after each deposition step. The rinse beakers contained 18 MΩ•cm high purity water. The time spent in each solution was 60, 30, 60, and 30 sec for the cationic, rinse, anionic, and rinse beakers respectively. The withdrawal and insertion rate was 1.8 mm/sec for all solutions. The deposition process was carried out at room temperature and humidity. For a description of the substrate preparation see chapter 2.4.A. in this thesis.

3.2.C. Solution and Thin Film Sample Analysis:

The UV-vis-spectrometer described in chapter 2.4.B. was used for the solutions of the various PDIs and the thin film bulk studies. The spectra obtained were background corrected for scattering using a macro (written in house) for the Igor graphing software package. The spectra were fitted to a double Gaussian and the absorbance maximum of the fit was recorded. Fluorescence spectra were recorded using the Fluoromax 2 fluorometer described in chapter 2.4.B of this thesis. The settings in all spectra were as follows: the excitation wavelength was 488 nm, the emission scan range was 500-700 nm, data was acquired in 1 nm increments, a 1 second integration time was used, and 1 nm slit widths were employed. An atomic force microscope (AFM) in tapping mode (AFM-TM) was used for analysis of the surface morphology and thickness of the films. A more detailed discussion on the AFM studies carried out in this thesis can be found in chapter 2.4.C.

3.2.D. Analysis of Surface Features and Thickness of Samples:

A more detailed description of the analysis of the surface features can be found in chapter 2.6.B.3 The surface features were analyzed using Lab View based software (written in house) to determine the fiber width.[14] The program gave the feature width in both the vertical and horizontal directions. The widths in each were averaged together to find the fiber width of the surface features. Equation 1 is used in this autocorrelation analysis.

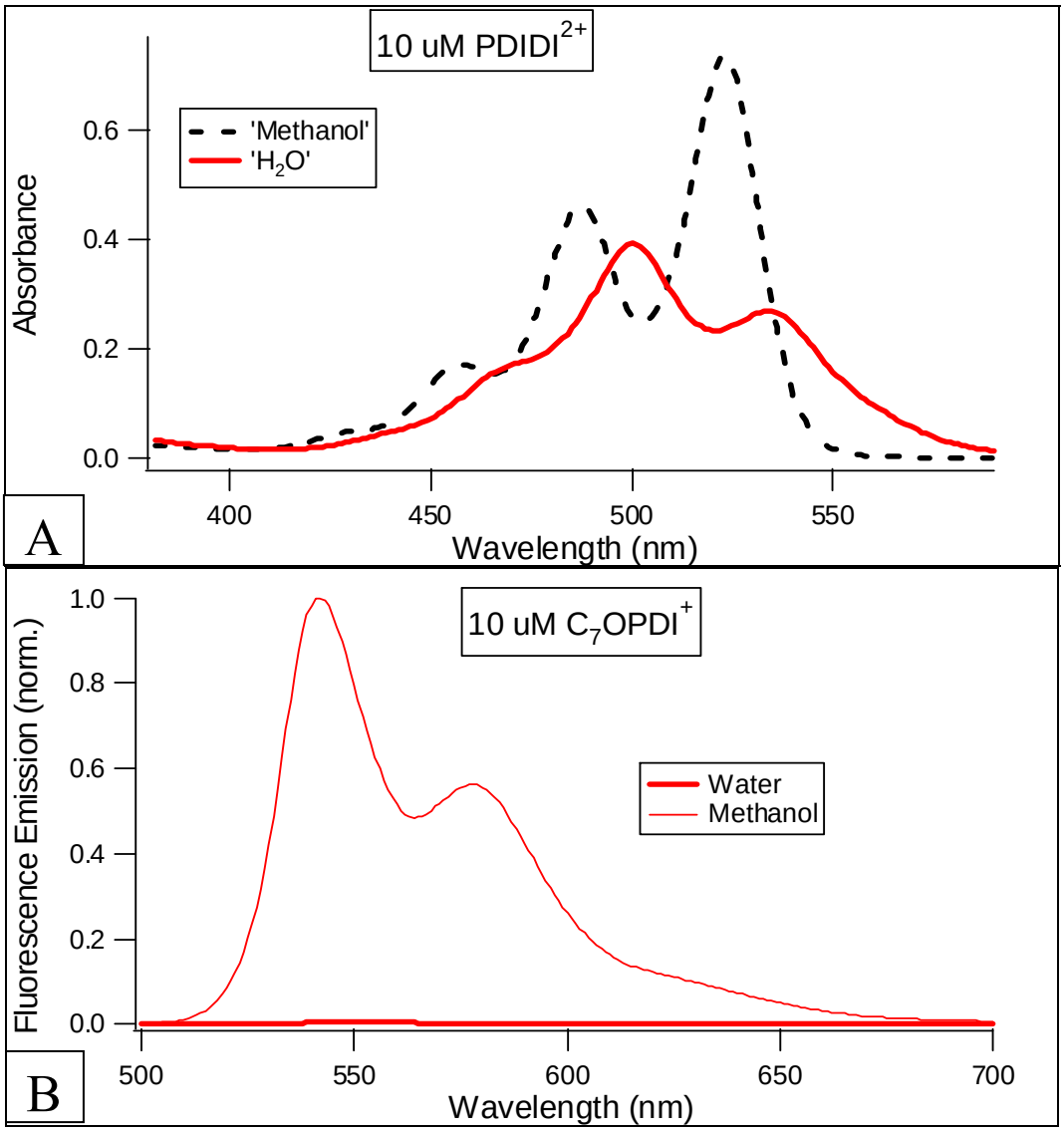

Figure 3.1. Absorbance and emission spectra

(A) UV-vis absorbance spectra for 10μM $PDIDI^{2+}$ in methanol and water. (B) The normalized emission spectra of a 10 μM C_7OPDI^{+} solution in methanol and water are shown. (C) Enlarged section of graph B showing the water spectrum.

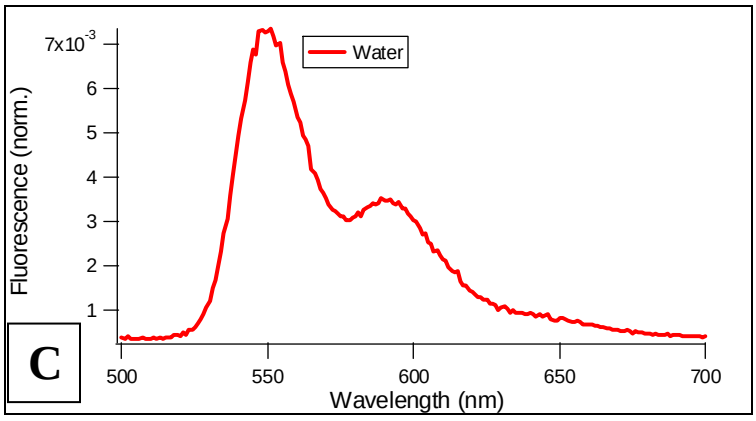

$$C(\xi,\varphi) = \frac{\langle h(x+\xi, y+\varphi)h(x,y)\rangle}{\langle h(x,y)\rangle^2}$$

Equation 3.1.Autocorrelation Function

In equation 3.1, h(x,y) represents the topographic height at the points x,y in the image. C(ξ,φ) is the autocorrelation function obtained. The brackets indicate a spatial average is taken during the calculation.

Thickness of the samples was determined in the following manner. First, the sample surface was scratched with a razor, removing the composite down to the substrate. The area containing the scratch was then imaged with the AFM. Then, a Lab View program (written in house) was used to determine the thickness of the samples. A more detailed discussion on the process involved in finding the depth and how the program works is given in chapter 2.6.B.4.

3.3. Results:

3.3.A. Bulk Properties:

The bulk solution properties of the PDIs were investigated to better understand their aggregation state. A representative absorption spectrum in methanol is shown in figure 1(A). This spectrum resembles the spectrum of the monomer, thus it is assumed that there is no aggregation of the PDIs in methanol.[15] A spectrum obtained in water can also be seen in figure 1(A), where an extreme shift in the spectrum is observed. This shows that aggregates are present in the precursor water solution. This aggregation can be assumed to be that of H-aggregates, based on the blue spectral shift.

$$\text{Fraction Aggregated} = \frac{I_{Max(methanol)} - I_{Max(water)}}{I_{Max(methanol)}}$$

Equation 3.2. Fraction Aggregated

In equation 3.2, $I_{max(methanol)}$ is the fluorescence intensity maximum for the PDI in the methanol. $I_{max(H2O)}$ is the fluorescence intensity maximum for PDI in dissolved in water.

In order, to classify the amount of aggregation in each precursor solution, the fraction aggregated was determined from the emission spectra in both methanol and water. The fraction aggregated was found by examining the fluorescence emission spectrum intensity in the two

solvents. The data were analyzed as shown in equation 2. The fluorescence spectrum of the C_7OPDI^+ in methanol and water is shown in figure 1(B, C). The fluorescence spectra of each are the same in shape and are assumed to be from the monomer.[16] The reduction in intensity is from self-quenching by the non-fluorescent aggregates formed.[17] The peak maximum of the various PDIs is shifted because of solvent effects. The fraction aggregated for each, when methanol and water are the solvents, was found to be 0.907, 0.993, and 0.972 for $PDIDI^{2+}$, C_7OPDI^+, and $PDISO_3^{2-}$ respectively.

3.3.B. Absorbance of Thin Films:

The PDI•PE composites displayed electrostatic LBL linear growth, as evidenced in figure 2. This is expected when there is a charge reversal situation present on the film surface.[14,18,19] The composite films are formed by the deposition of aggregates as demonstrated by the similarity between the composite's and the precursor's absorbance spectrum solution. The deposition of the stacked form of PDI on the surface of thin films was previously seen in literature.[17] The C_7OPDI^+•PA^- films showed greater film growth as evidenced by the absorbance vs. bilayer in figure 1(B). The absorbance per bilayer is found to be 0.0698, 0.0419, and 0.0401 for C_7OPDI^+•PA^-, $PDIDI^{2+}$•PA^-, and $PDISO_3^{2-}$•$PDDA^+$ respectively. This demonstrates a direct relationship between fraction aggregated in the precursor solution and the deposition rate. The larger the fraction aggregated in the precursor solution, greater the chance for aggregate deposition on the surface. Also, the results found here give an indication that hydrophobic forces control deposition more than electrostatic forces. This is observed in how the C_7OPDI^+•PA^- thin films composites grew the fastest. The LBL growth was still observed. When compared to the absorbance per bilayer found by Webber, the compounds used here deposited at a faster rate.[19]

3.3.C. Morphology of Thin Films:

3.3.C.1. Morphology of $PDISO_3^{2-}$•$PDDA^+$ Thin Films:

The surface morphology of the $PDISO_3^{2-}$•$PDDA^+$ composites was investigated by AFM. The $PDISO_3^{2-}$•$PDDA^+$ composite films prepared are compared show tightly curled fibers on the surface. Representative images of the bilayer films can be seen in figure 3. Films with fewer bilayers have narrow tightly curled fibers that intertwine as shown in figure 3 (A, B). An increase in bilayer number causes the fibers to get thicker and lose the tightly curled structure.

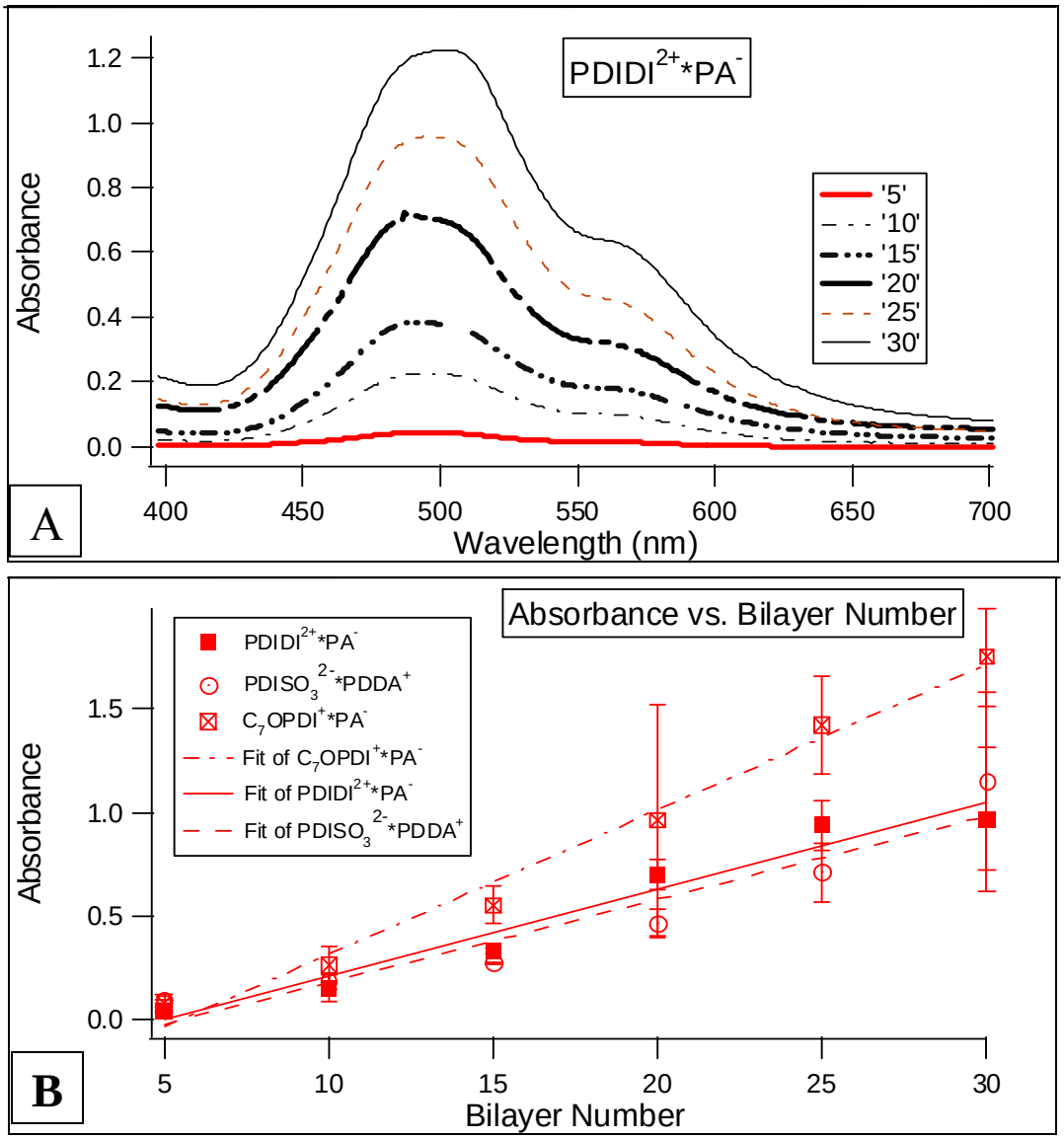

Figure 3.2. Absorbance Spectra vs. Wavelength and (B) Absorbance spectra vs Bialyer number.

(A) Absorbance spectra of the $PDIDI^{2+}$•PA^{-} composites as a function of bilayer number. (B) Displays the absorbance vs. bilayer number for all three types of composites looked at. A linear fit is preformed on each set of data points for the three different composites.

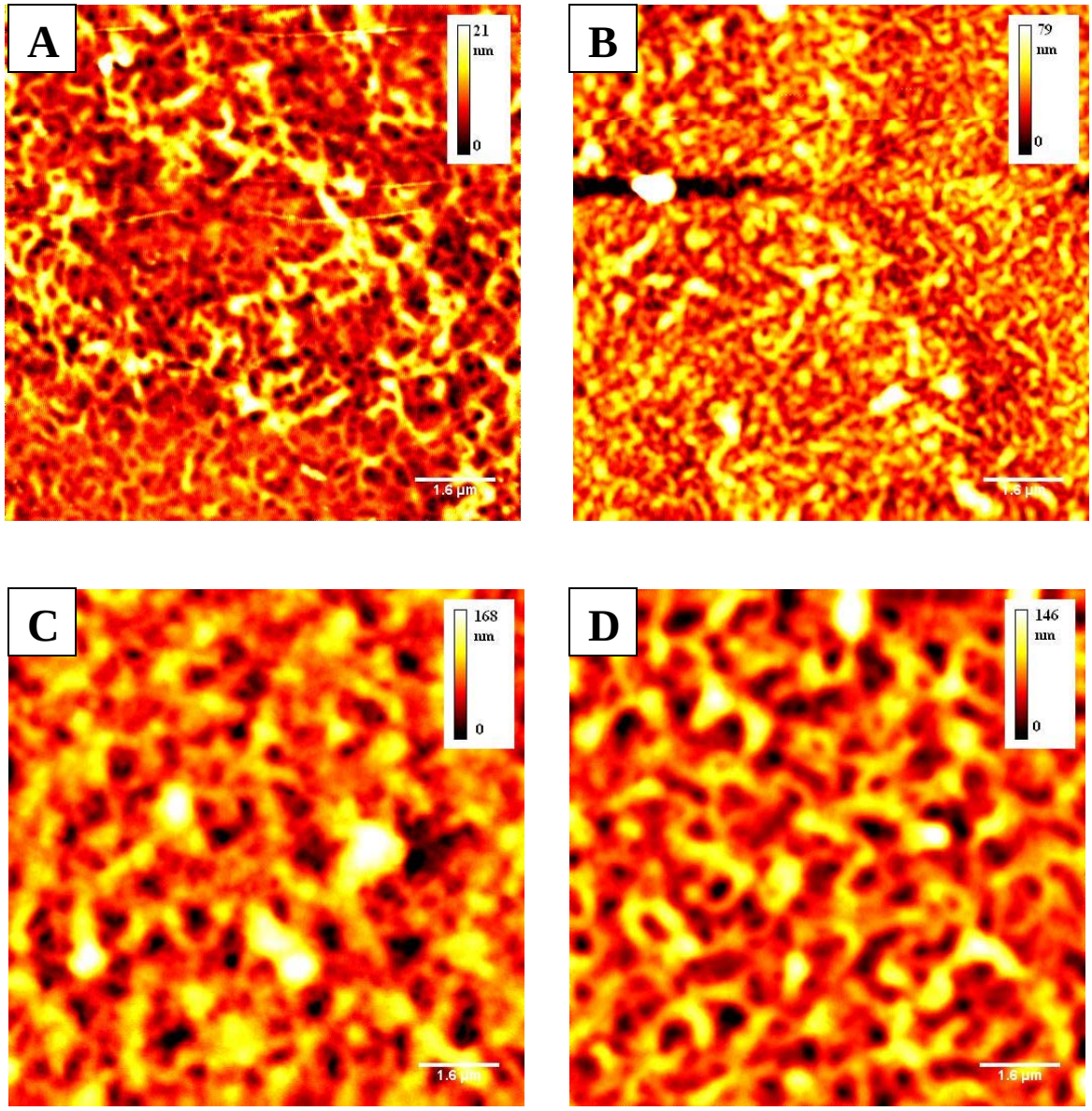

Figure 3.3. AFM images $PDISO_3^{2-}$•$PDDA^+$ thin film composites

This shows representative AFM images of $PDISO_3^{2-}$•$PDDA^+$ (10 x 10 µm) at a scan rate of 10 µm/sec. The number of bilayers is (A) 10, (B) 15, (C) 25, and (D) 30 respectively. Scale bars and calibration bars are shown for each image.

The loss of the tightly curled structure is due to the fibers grafting together with increasing deposition cycles. The increase in number of bilayers deposited resulted in thicker fibers where in some locations oval domains existed at ends of the fibers in the 30 bilayer composite films, as shown in figure 3(D). The feature height increases with the bilayer number, as seen in the calibration bars of the images in figure 3.

The fiber width was investigated quantitatively by performing an autocorrelation on the images. The fiber widths get larger as bilayer number is increased, as shown in figure 4(A). The 10 bilayer films displayed fiber widths of approximately 360 nm compared to the 30 bilayer sample where the fiber width approached 775 nm. This trend follows the theory where the initial fibers act as nucleation sites for further growth.

The film thickness also increases with bilayer number. The thickness of the samples went from 48 nm at 10 bilayers to 111 nm and 408 nm at 20 and 30 bilayers respectively. The thicknesses for the $PDISO_3^{2-}$•$PDDA^+$ composites created are displayed in figure 5. The increase in film thickness with an increase in bilayer number demonstrates effective LBL growth, as observed in charge reversal situations.[20] Taken together, the absorbance, fiber width and film thickness data demonstrate that LBL methods allow for molecular scale control over film properties in these composites.

3.3.C.2. Mechanism of Fiber Growth:

The mechanism of fiber growth was proved to be similar to the mechanism explained previously.[14] The fibers are shown to grow by initial aggregate deposition on the substrate resulting in charge reversal on the surface. This charge reversal favors further electrostatic growth. The next deposition of oppositely charged solution results in chances for the PDI or PE to deposit on a surface where the charge has been reversed. These initial segments would then have either more PE or PDI deposit on them at the initial surface aggregation sites. The sites then have the π-π stacked aggregates arrange on the ends of the initial sites forming longer fibers. The primary mechanism in the continuation of film growth is the electrostatic attraction of the different layers, as previously reported with similar PDIs.[14] This was proven by how the films display no growth without the oppositely charged precursor solution. These initial fibers continue to get thicker and higher resulting in fibers grafting together and overlapping. This causes the alteration of the initial fiber appearance, with the loss of fiber structure.

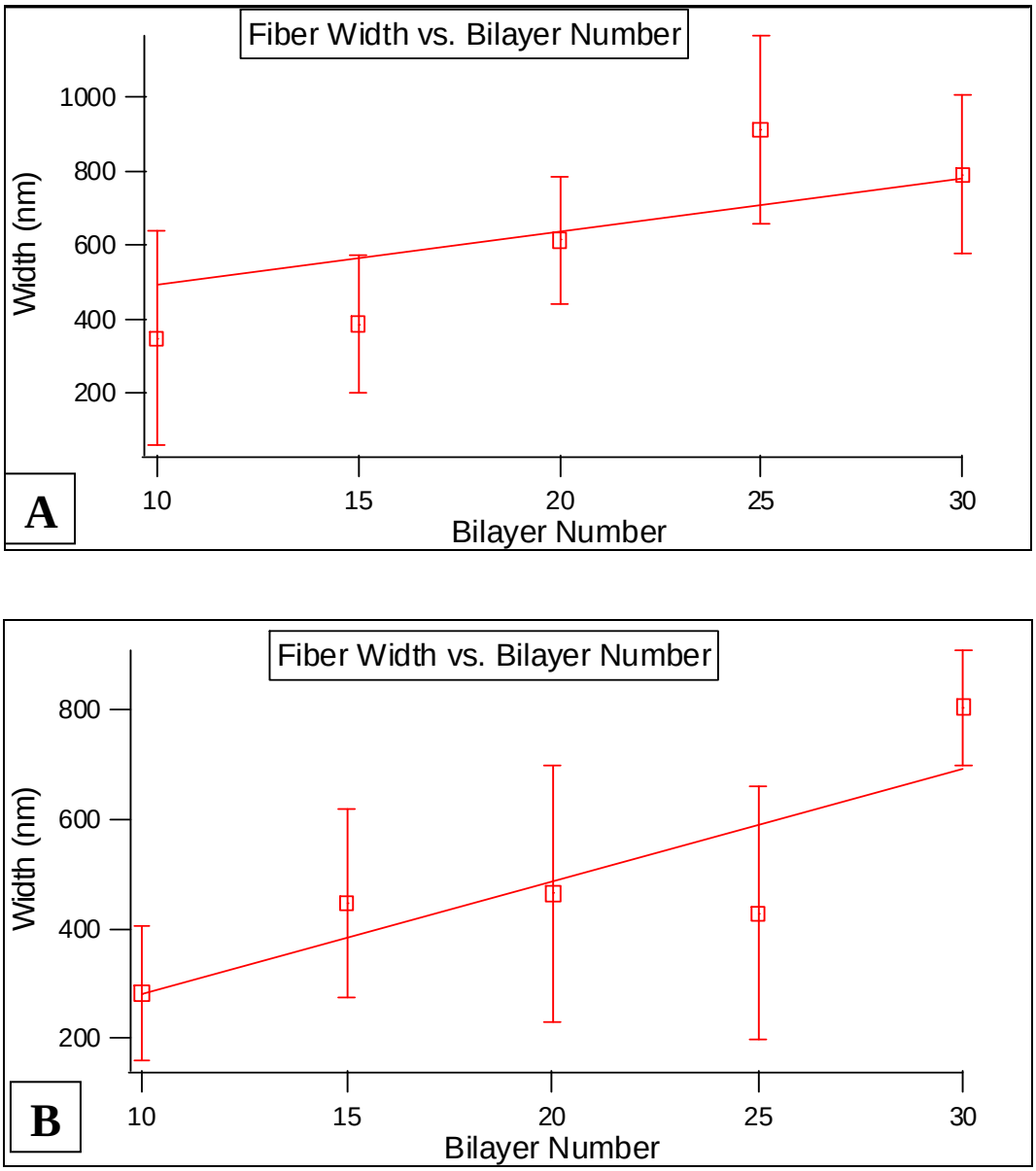

Figure 3.4. (A) Fiber width $PDISO_3^{2-}$•$PDDA^+$ vs. bilayer number and (B) fiber width $PDIDI^{2+}$•PA^- vs. bilayer number

(A) Average fiber width for three of the AFM images as a function of bilayer number is shown for the $PDISO_3^{2-}$•$PDDA^+$ composites. (B) The average fiber width for three of the AFM images as a function of the bilayer number for the $PDIDI^{2+}$•PA^- composite.

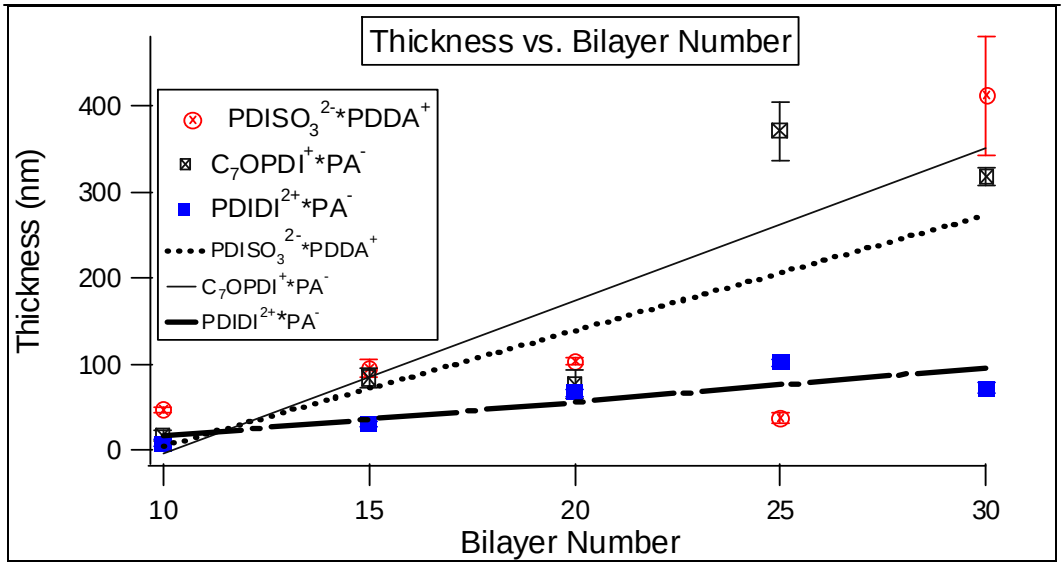

Figure 3.5. Thickness vs. Bilayer Number

Thickness of the composites as a function of bilayer number for all the thin films made. The standard deviation is shown at each data point, determined from 3 replicate measurements.

3.3.C.3. Morphology of PDIDI^{2+}•PA^{-}:

The surface morphology of PDIDI^{2+}•PA^{-} composite thin films was also examined by AFM imaging. These films exhibit randomly curved fibers for the 10 and 15 bilayer films shown in figure 6(A, B). These morphed into straighter connected islands where some of the underlying fiber structure is still observed, as evidenced in figure 6 (C, D). The ten bilayer and higher samples had consistent film appearance at all the locations imaged. The AFM images clearly show evidence of fiber growth leading to larger structures.

The fiber widths of the composites showed an increase with bilayer number, as seen in figure 4(B). The width of the fibers was found to be 445 nm for the 15 bilayer film. The fiber widths of the 15, 20, and 25 bilayer samples were similar with a large change in the 30 bilayer sample. The 30 bilayer sample was 2.5 times larger than the 10 bilayer sample, demonstrating an approximately linear increase in fiber width, with bilayer number.

The increase in thickness was found to be two fold greater when the bilayer number doubled, as observed in figure 5. Also, this showed the thickness increased with bilayer number, as observed earlier in the PDISO$_3^{2-}$•PDDA^{+} composite. This is also observed in other charge reversal situations.[19] The LBL process here again displayed control of thickness just like in the PDISO$_3^{2-}$•PDDA^{+} composite thin films. This can be predicted, when all the other deposition

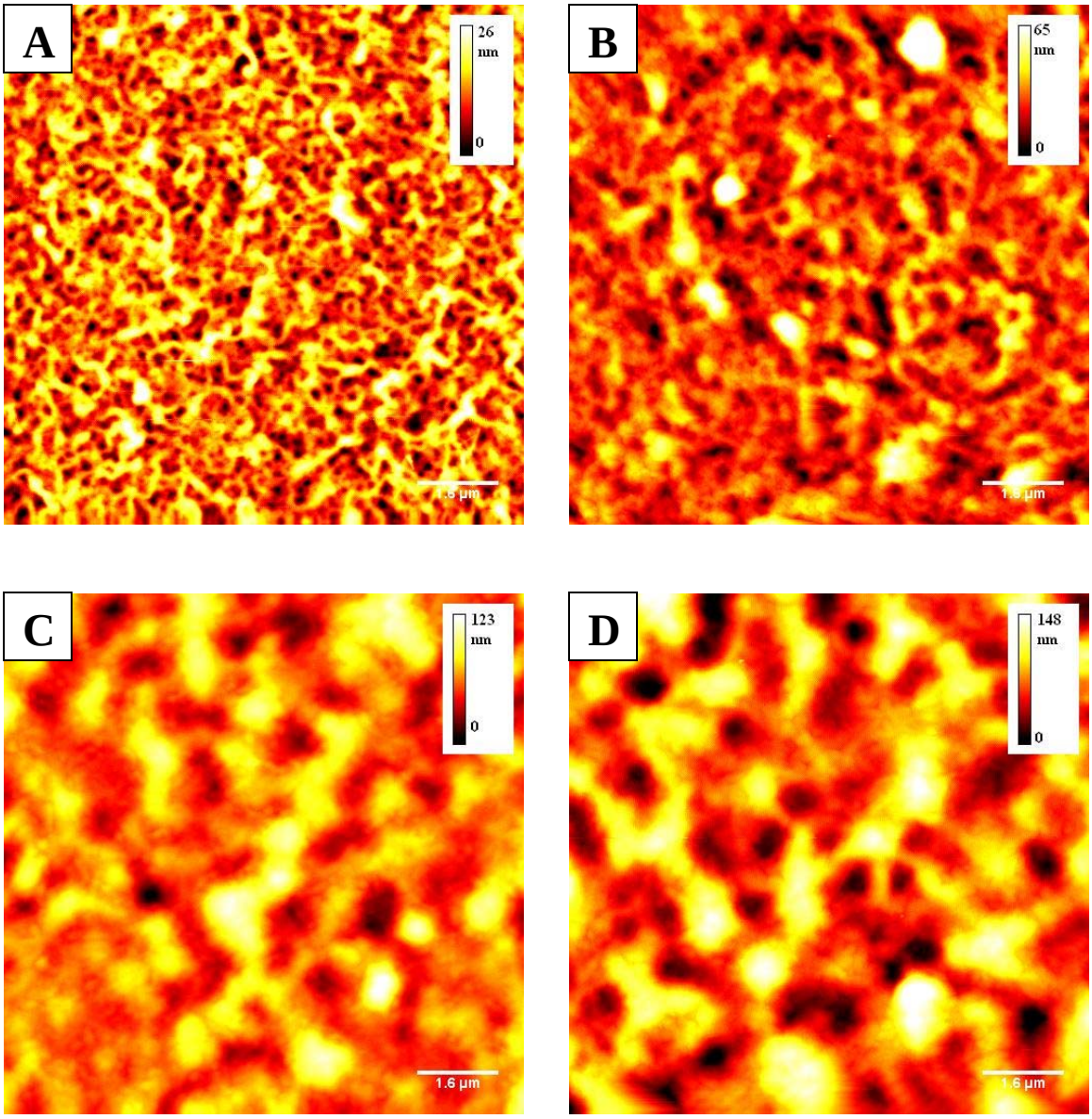

Figure 3.6 AFM Images of the $PDIDI^{2+}$•PA^{-} Thin Films

AFM images of $PDIDI^{2+}$•PA^{-} (10 x 10 µm) recorded at a scan rate of 10µm/sec. The numbers of bilayers are (A) 10, (B) 15, (C) 25, and (D) 30, respectively. The thin films were deposited at room temperature and humidity. The deposition was done carried out by deposition in $PDIDI^{2+}$, rinse beaker, PA^{-}, and rinse beakers with hold times of 60, 30, 60, and 30 seconds respectively.

conditions are held constant. However, the thickness varied only slightly from an exact linear increase with bilayer number in this composite thin film compared to the $PDISO_3^{2-}$•$PDDA^+$ samples.

3.3.C.4. Morphology of C_7OPDI^+•PA^-:

The surface morphology of the C_7OPDI^+•PA^- composite thin films was also explored by AFM imaging. The films showed wavy thin fibers with directional alignment present. The surface features in the 10 and 15 bilayer samples clearly showed directional growth of the fibers, as evident in figure 7 (A, B). The surface features showed drastic changes in morphology for 20 bilayer and thicker composites. These fibers still appeared to incorporate some directional alignment in them, between the large straight fibers. In these latter samples, the fibers have overlapped and grown together forming large straight fiber mounds. The large straight fiber mounds are most apparent in the 30 bilayer sample, as shown in figure 7(D). By comparing the calibration bars for the images shown, the surface feature height is seen to triple when bilayer number doubles.

The autocorrelation program, mentioned earlier in section 3.3.D and described in detail in chapter 2, was used to examine the fiber width. The fibers found in 10 to 15 bilayer composites had widths of 323 nm and 343 nm respectively, as seen in figure 8. Here, fiber width was plotted from the average of three images for each sample. The 25 bilayer sample displayed a fiber width of over twice that of the 15 bilayer composite. The 30 bilayer film displayed the largest fiber width as expected. This trend is what is expected as more material gets deposited.

The thickness of the samples also increases with an increase in bilayer number. This increase was clearly present at 10 bilayer increments, as observed in figure 5. The 25 and 30 bilayer samples showed a large increase with thickness over 300 nm for each compared to the 10 and 20 bilayer samples, which were 13 and 91 nm thick. This randomized thickness increase could be explained by variations from sample to sample in location of scratch. However, the trend observed is still an overall increase in the film's thickness with bilayer number.

3.3.D. Comparison of PDI Films:

The three different PDI•PE composites create unique fiber structures when prepared as thin films. When the ten bilayer samples of all three are examined, there are some fine differences in the film morphology. The $PDISO_3^{2-}$•$PDDA^+$ composite has highly curved

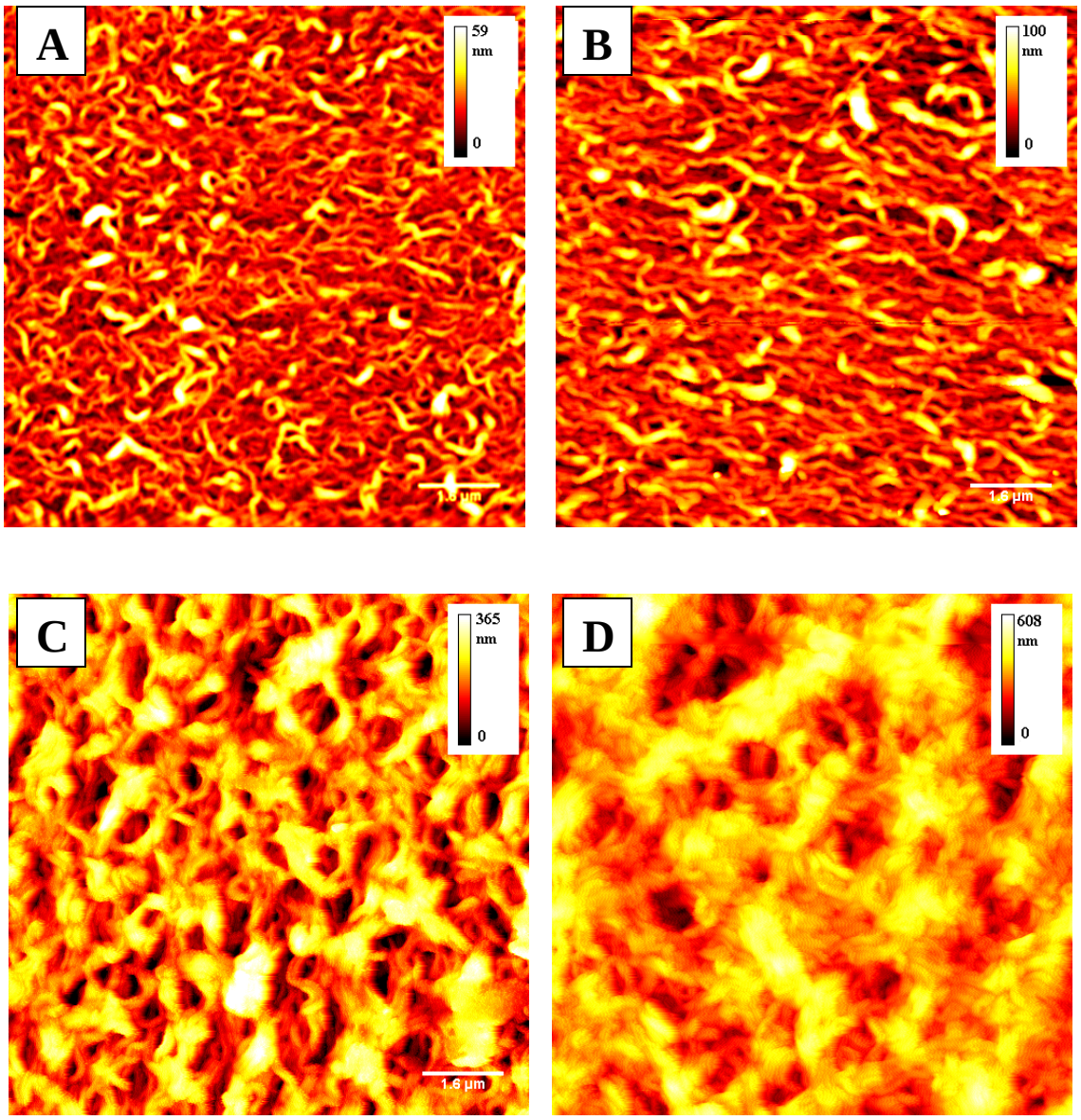

Figure 3.7 AFM Images $C_7OPDI^+•PA^-$ Thin Films

AFM images (10 x 10 µm) at a scan rate of 10 µm/sec. The $C_7OPDI^+•PA^-$ films with (A) 10, (B) 15, (C) 25, and (D) 30 bilayers, respectively. The composite films were created by deposition of C_7OPDI^+, rinse, PA^-, and rinse solutions with hold times of 60, 30, 60, and 30 seconds respectively. The withdrawal rate for the substrate into and out of the solution was 1.8 mm/second.

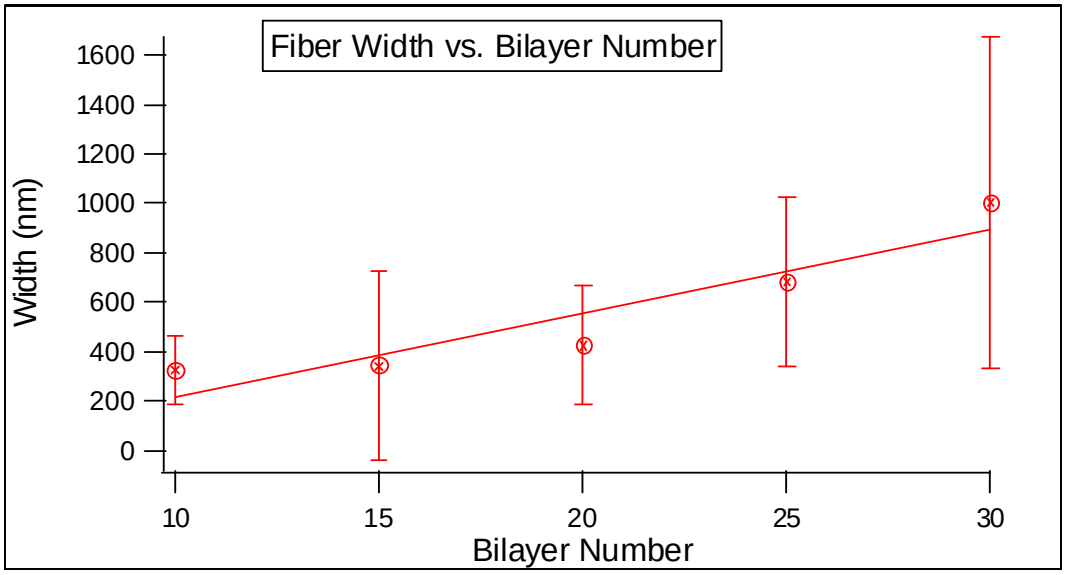

Figure 3.8 Width of $C_7OPDI^+•PA^-$ Fibers

The average fiber width vs. bilayers for the $C_7OPDI^+•PA^-$ composites are shown. The standard deviation is shown for each bilayer number.

intertwined fibers, compared to the $PDIDI^{2+}•PA^-$ composite. The $C_7OPDI^+•PA^-$ composite does not display curved fibers; instead the fibers are narrow and straighter, exhibiting directional alignment. The symmetrically charged PDIs in the composite favor a highly curved fiber structure compared to the asymmetric $C_7OPDI^+•PA^-$ composite, where wavy fibers appear to be present. Three different 20 bilayer PDI•PE composites films are displayed in figure 9. Here, distinct differences exist between the three. The $PDISO_3^{2-}•PDDA^+$ composite has a distinct curved fibers present. The $PDIDI^{2+}•PA^-$ composite appears less fiber like with thicker fibers and greater degree in variation in the height of the fibers. The $C_7OPDI^+•PA^-$ has smaller bundled fibers, which turn into mounds, which display some sign of alignment. The three composites all show signs of grafting together after 15 bilayers, where the distinct fiber structures become thicker and changes from the fibers initial appearance. The loss of distinct fiber structure is caused by the fibers grafting together, producing thicker and higher structures by overlapping and joining of the fibers, see section 3.3.B.2. The dissimilarities in the initial fibers result in thicker fibers of less curled structure in the final films ($PDIDI^{2+}•PA^-$), compared to how wavy fibers lead to large fibers with mounds in the case of $C_7OPDI^+•PA^-$ composites.

The thickness of the films all showed an increase with bilayer number. There was however a noticeable difference in the maximum thickness of the three films. This is readily

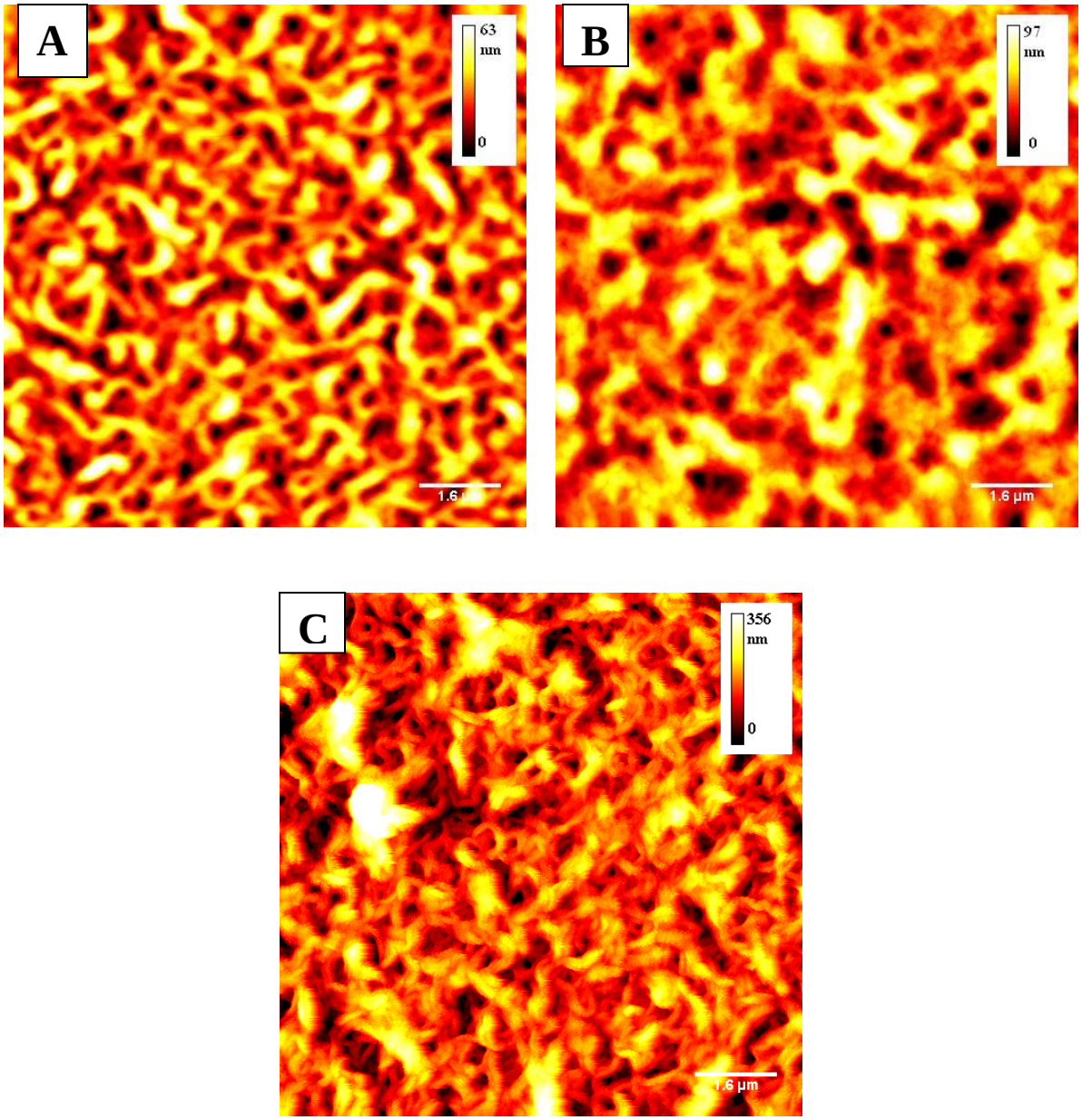

Figure 3.9. AFM Images 20 Bilayers

AFM images are shown for (A) $PDISO_3^{2-}$•$PDDA^+$, (B) $PDIDI^+$•PA^-, and (C) C_7OPDI^+•PA^- thin film composites. Each image is of a 10 x 10 µm region, all three are for 20 bilayer samples and all were prepared under identical conditions.

seen in figure 5 with the thickest films being 408 and 392 nm for $PDISO_3^{2-}$•$PDDA^+$ and C_7OPDI^+•PA^- respectively with the $PDIDI^{2+}$•PA^- composite being only 149 nm thick. This also occurs with the 10 bilayer samples where thickness of the $PDIDI^{2+}$•PA^- composite was again half the width of the other two. The largest differences between the $PDIDI^{2+}$•PA^- and $PDISO_3^{2-}$•$PDDA^+$ composite lay in the polyelectrolyte molecular weight. The molecular weight of $PDDA^+$ and PA^- are in the range of 100,000-200,000 and 5,100 respectively. The significant difference in the molecular weights of the PEs easily explains the thickness differences observed in the two composite films. There happens to be more $PDDA^+$ going down for each polyelectrolyte being absorbed down on the film. The C_7OPDI^+•PA^- composite is thicker compared to $PDIDI^{2+}$•PA^- and about equal to the $PDISO_3^{2-}$•$PDDA^+$ film. This along with the fraction bound data indicates more aggregates are present in the precursor solution for the C_7OPDI^+•PA^- composites.

3.4. Conclusion:

Studies of the effects three water-soluble PDIs have on thin film growth and morphology were executed. Growth was observed via electrostatic deposition of aggregate on the substrate. Deposition was found to depend linearly on the number of bilayers deposited. The more aggregated C_7OPDI^+ was observed to more readily deposit onto the substrate surface. The film morphology also displayed the effects of the more aggregated C_7OPDI^+•PA^- composite incorporating wavy fibrous structures at the lower bilayer numbers of 10 and 15, compared to the highly curled fibers in the symmetric PDIs. The asymmetric water-soluble PDI resulted in fibers with possible alignment. The effects of the greater aggregation of the C_7OPDI^+•PA^- composite could also be observed in how the films thickness was similar to the $PDISO_3^{2-}$•$PDDA^+$ composite, which used a polyelectrolyte with a higher molecular weight. The three different composites all showed the trend of fiber widths increasing as bilayer number and after a certain point, loss of initial fiber structure in favor of thicker fibers and other features. The 20 bilayer films are at the point where enough of the fibers have grown together to cause loss of directionality. The composite films created have potential uses in organic field effect transistors.[21] Investigations into other asymmetric PDIs for determination of the effect on alignment at low bilayer numbers could be investigated, perhaps resulting in increase order for fabricated organic transistors and other devices.

References:

[1] Lu, W., Gao, J. P.; Wang, Z. Y.; Qi, Y.; Sacripante, G. G.; Duff, J. D.; Sundararajan, P. R. *Macromolecules* **1999**, 32, 8880.

[2] Ego, C.; Marsitzky, D.; Becker, S.; Zhang, J.; Grimsdale, A. C.; Müllen, K.; Mackenzie, J. D.; Silva, C.; Friend, R. H. *J. Am. Chem. Soc.* **2003**, 125, 437.

[3] Loewe, R. S.; Tomizaki, K.-Y.; Youngblood, W. J.; Bo, Z.; Lindsey, J. S. *J. Mater. Chem.* **2002,** 12, 3438.

[4] Kudo, T.; Kimura, M.; Hanabusa, K.; Shirai, H. *J. Porphyrins Phthalocyanines 2* **1998**, 2, 231.

[5] Li, J.; Dierschke, F.; Wu, J.; Grimsdale, A. C.; Müllen, K. *J. Mater. Chem*. **2006**, 16, 96.

[6] An, Z.; Yu, J.; Jones, S.C.; Barlow, S.; Yoo, S.; Domercq, B.; Prins, P.; Siebbeles, L. D. A.; Kippelen, B.; Marder, S. R. *Adv. Mater*. **2005**, 17, 2580.

[7] Balakrishnan, K.; Datar, A.; Oitker, R.; Chen, H.; Zuo, J.; Zang, L. *J. Am. Chem. Soc*. **2005**, 127, 10496.

[8] Weiss, E. A.; Ahrens, M. J.; Sinks, L. E.; Gusev, A. V.; Ratner, M. A.; Wasielewski, M. R. *J. Am. Chem. Soc*. **2004**, 126, 5577.

[9] Hosoi, Y.; Tsunami, D.; Ishii, H.; Furukawa, Y. *Chem. Phys. Lett*. **2007**, 436, 139.

[10] Decher, G. *Sciene* **1997**, 277, 1232.

[11] Paloniemi, H.; Lukkarinen, M.; Ääritalo, T.; Areva, S.; Leiro, J.; Heinonen, M.; Haapakka, K.; Lukkari, J. *Langmuir* **2006**, 22, 74.

[12] Huang, S. C. J.; Artyukhin, A. B.; Wang, Y.; Ju, J.-W.; Stroeve, P.; Noy, A. *J. Am. Chem. Soc*. **2005**, 127, 14176.

[13] Song, Y.; Kim, G. Y.; Choi, H. K.; Jeong, H. J.; Kim, K. K.; Yang, C. M.; Lim, S. C.; An, K. H.; Jung, K. T.; Lee, Y. H. *Chem. Vap. Deposition* **2006**, 12, 375.

[14] Everett, T. A.; Twite, A. A.; Xie, A.; Battina, S. K.; Hua, D. H.; Higgins, D. A. *Chem. Mater*. **2006**, 18 (25), 5937.

[15] Herrikhuyzen, J.; Syamakuri, A.; Schennig, A. P. H. J., Meijer, E. W. *J. Am. Chem. Soc*. **2004**, 126, 10021.

[16] Balakrishnan, K.; Datar, A.; Naddo, T.; Huang, J.; Oitker, R.; Yen, M.; Zhao, J.; Zang, L. *J. Am. Chem. Soc*. **2006**, 128, 7390.

[17] Marcon, R. O.; Santos, J. G.; Figueiredo, K. M.; Brochsztain, S. *Langmuir* **2006**, 22, 1680.

[18] Tang, T.; Qu, J.; Müllen, K.; Webber, S. E. *Langmuir* **2006**, 22, 26.

[19] Tang, T.; Qu, J.; Müllen, K.; Webber, S. E. *Langmuir*, **2006**, 22, 7610.

[20] Chiarelli, P. A.; Johal, M. S.; Holmes, J. D.; Casson, J. L.; Robinson, J. M.; Wang, H. *Langmuir* **2002**, 18,168.

[21] Hosoi, Y.; Tsunami, D.; Ishii, H.; Furukawa, Y. *Chem. Phys. Lett.* **2007**, 436, 139.

CHAPTER 4 - Nanofiber Growth and Alignment by Electrostatic Self-Assembly of Perylene Diimide•Polyelectrolyte Composite Thin Films

4.1. Introduction:

P-type organic semiconductors have seen limited success in producing high performance organic thin film transistors (OTFTs). One such OTFT built with pentancene has shown field effect mobility equal to or greater than amorphous silicon.[1,2,3,4] This has lead to an increase in studies of complimentary n-type organic semiconducting materials. The main problem exhibited by many of the n-type organic semiconducting materials is sensitivity to air. There are however some n-type organic semiconductor molecules that do not degrade in air; perylene diimides (PDIs) are one such example.[5] PDIs and their derivatives have been examined for a wide range of applications, with one application being the formation of nanowires.[6] A complete understanding of how PDIs form thin films and other useful structures such as nanowires is of importance to their future application in electronic devices. Many different applications exist for which nanowires could be used, such as in flexible lightweight electronic circuitry. Thin films and other organic semiconductor based devices are often formed from solutions where the materials are dissolved in harsh solvents. Many PDIs must be cast from these same harsh solvents. Recently however, a series of water-soluble PDIs have been developed that have displayed excellent LBL growth properties.[7,8,9,10]

The use of electrostatic-self-assembled (ESA) materials in a layer-by-layer (LBL) method with alternating cationic and anionic solutions has been shown to be an effective means for preparing semiconductor thin films.[11] The use of ESA-based methods provides a way to precisely control growth of thin films. Water-soluble PDIs are charged molecules, which can be used in ESA-based LBL processes. The PDIs studied previously have shown excellent fiber growth.[10] However, the materials were produced in a predominately non-aligned fashion.[10,12] In chapter 3, three different types of PDIs were examined, two symmetric substituted, and an asymmetric PDI in N-(butoxypropyl)-N'-(2-(N,N,N-trimethylammonio)ethyl) perylene-3, 4,9,10-tetracarboxylic diimide iodide (C_7OPDI^+). The C_7OPDI^+ was the exception, showing

signs of directional growth, unlike the other PDIs examined in this thesis. The alignment of fibers in a controlled direction will be examined further in this chapter. The development of methods for preparing aligned nanofibers would prove to be of huge importance if realized. This would lead to applications of such organic nanowires in efficient thin film transistors, for example.

It is believed fiber alignment will occur along and parallel to the dipping direction. The deposition process will utilize a dip coater to insert the substrate and hold it in the precursor C_7OPDI^+ and poly(acrylic acid) (PA^-) solutions. The dip coater will control the time the substrate spends in each solution, the withdrawal rate, and how much of the substrate is exposed to the precursor deposition solutions, thus the dip coater can be effectively used to control the growth of $C_7OPDI^+ \cdot PA^-$ composites.

4.2. Experimental:

4.2.A. Synthesis of Starting Products and Precursor Solutions:

The synthesis of the starting material N-(butoxypropyl)-N'-(2-(N,N,N-trimethylammonio)ethyl) perylene-3,4,9,10-tetracarboxylic diimide iodide (C_7OPDI^+) is fully covered in chapter 2. The preparation of the precursor solutions can be found in chapter 2 for both the C_7OPDI^+ and the PA^- precursors. The solutions prepared were 206 μM C_7OPDI^+ in 18 MΩ•cm high purity water and 3 mM PA^- in 0.1 M phosphate buffer (pH 7). The glass cover slips, which were used as the thin film substrate, were plasma cleaned prior to film deposition.

4.2.B. Solution Studies:

Solution studies were utilized to determine if the C_7OPDI^+ was present in a monomeric or aggregated form. The solution studies involved preparation of 10 μM C_7OPDI^+ solutions. This was done by taking 1.214 mL of the stock 206 μM solution and transferring it to 2, 25 mL volumetric flasks. These flasks were then diluted to volume with either methanol or high purity water.

4.2.C. Thin Film Formation:

ESA-based LBL deposition was carried out by use of a linear dip coater, as previously described in chapter 2 of this thesis. The dip coater provided an automated way to control the

deposition time, withdrawal rate, and number of bilayers deposited. The dip coater was enclosed in Plexiglas for protecting the deposition solutions from dust and other environmental contaminants. The deposition involved exposure of the substrate to the following four solutions: C_7OPDI^+, high purity water, PA^-, and high purity water. The time during which the glass cover slip was held in each dipping solution was 60, 30, 60, and 30 seconds respectively. The dip coater withdrew and inserted the substrate at a rate of 1.8 mm/sec.

4.2.D. Characterization of Precursor Solutions and Thin Films:

Characterization of the precursor solutions and thin films obtained was accomplished by UV-vis spectroscopy, fluorescence spectroscopy, and atomic force microscopy, the latter operating in tapping mode (AFM-TM). The UV-vis spectrometer was used to determine the absorbance for both the solution and thin film composite samples. The fluorometer was used for emission detection for the solution studies. In all spectra, the excitation wavelength was 488 nm, the emission scan range was 500-700 nm, data was acquired at 1 nm increments, a 1 sec. integration time was used, and 1 nm slit widths were employed. The AFM-TM was utilized for determination of the morphology and thickness of the films.

Film thickness, fiber width, and fiber alignment was examined by the use of a Lab View Program (written in house). Determination of the thickness of the samples involved use of a razor to remove the composite down to the substrate. The samples were then imaged in this region; the height of the film edge directly determined the thickness. The procedures employed were fully explained in chapter 2.

4.3. Results:

4.3.A. Bulk Studies:

The aggregation state of the C_7OPDI^+ in the precursor solution was determined by absorbance and fluorescence measurements. The absorbance spectrum of C_7OPDI^+ in methanol can be seen in figure 1(A) with a peak maximum at 522 nm. The spectrum displayed in methanol is that of the monomer. When the C_7OPDI^+ is dissolved in water a dramatic change in the spectrum is observed, as seen in figure 1(A). The difference observed in these spectra indicates a change in the state from the monomer to an aggregated state, with a peak maximum

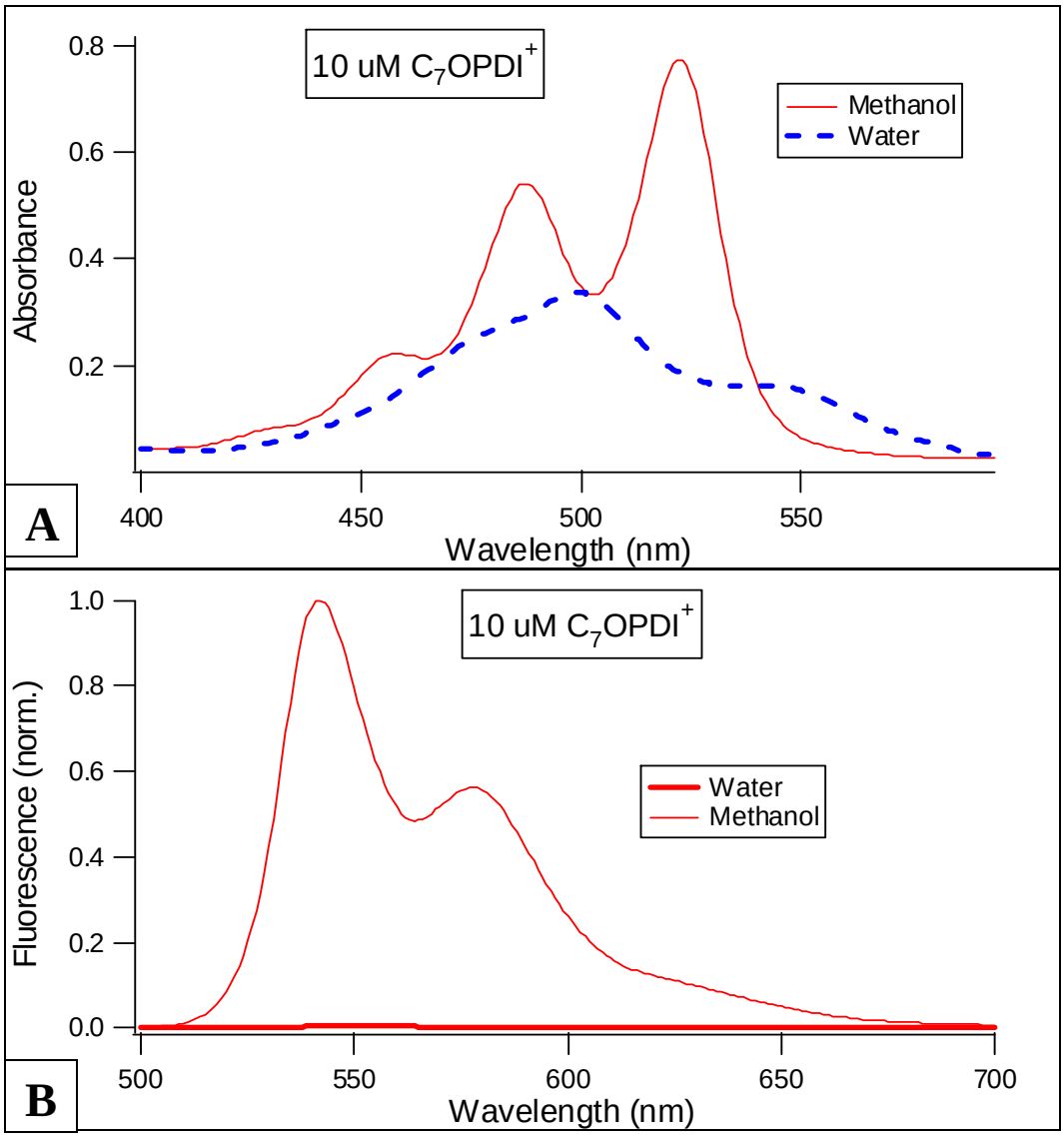

Figure 4.1. Absorbance and emission spectra of C_7OPDI^+

(A) UV-vis absorbance spectra for 10 µM C_7OPDI^+ is shown in both water and methanol. (B) The normalized emission spectra for 10 µM C_7OPDI^+ in both water and methanol. (C) Enlarged section of graph B showing the water spectrum.

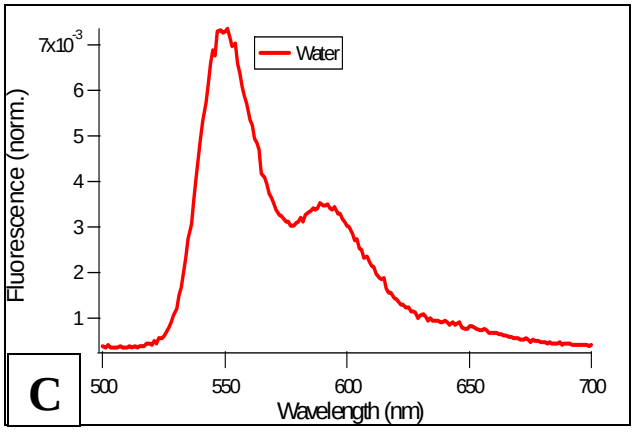

of 500 nm. The shift in the absorbance spectra is a result of the π-bonds overlapping, when the molecules aggregate together. The spectral shift observed show similarities to H aggregates.

In order to determine how much of C_7OPDI^+ is in the aggregated state when in an aqueous solution, the fluorescence emission spectra obtained in water and methanol were also compared. The emission spectrum in methanol is assumed to be due only to the monomer. The spectrum observed when the solvent is water is noted to also be that of the monomer, as evidence by its similar appearance (see figure 1(B,C)). The slight difference in emission maximum for the two is from the solvent effects. The difference in intensity between these two spectra comes from the amount of C_7OPDI^+ present in the aggregated state in the aqueous solution. The reduction in intensity is a result of self-quenching of the aggregates, which are non-fluorescent.[13] This gives a clear indication of the aqueous precursor solutions are primarily comprised of C_7OPDI^+ aggregates. From the two normalized emission intensities in methanol and water, the fraction aggregated in the aqueous solution can be found. The fraction aggregated was found to be 0.997. This number indicates that the majority of the dye is found in the aggregated state.

4.3.B. Alignment in the Composite Films:

The absorbance spectra obtained from $C_7OPDI^+ \bullet PA^-$ composite thin films are similar in appearance to the solution spectrum of the aggregated dye, indicating aggregates are deposited from solution during film deposition. An increase in the thin film absorbance with bilayer number is observed. Such behavior is classically observed in electrostatic LBL processes.[7] To detect alignment in the bulk material, the absorbance dichroism of each sample was determined. A detailed explanation of these measurements is given in chapter 2. Briefly, the absorbance was simply obtained with light polarized parallel and perpendicular to the dipping direction in these experiments. Representative spectra can be observed in figure 2(A). The peak maximum was the same for both polarizations, and appeared at 481 nm. The absorbance obtained for both polarizations was found to increase with bilayer number. The difference between the two also appeared to widen a little, as shown in figure 2(B). The observed difference in absorbance for the two polarizations is a clear indication of bulk alignment in the films. This result suggests the long axis of the PDI molecules align perpendicular to the dipping direction. The reasons behind such an alignment will explained later in this chapter.

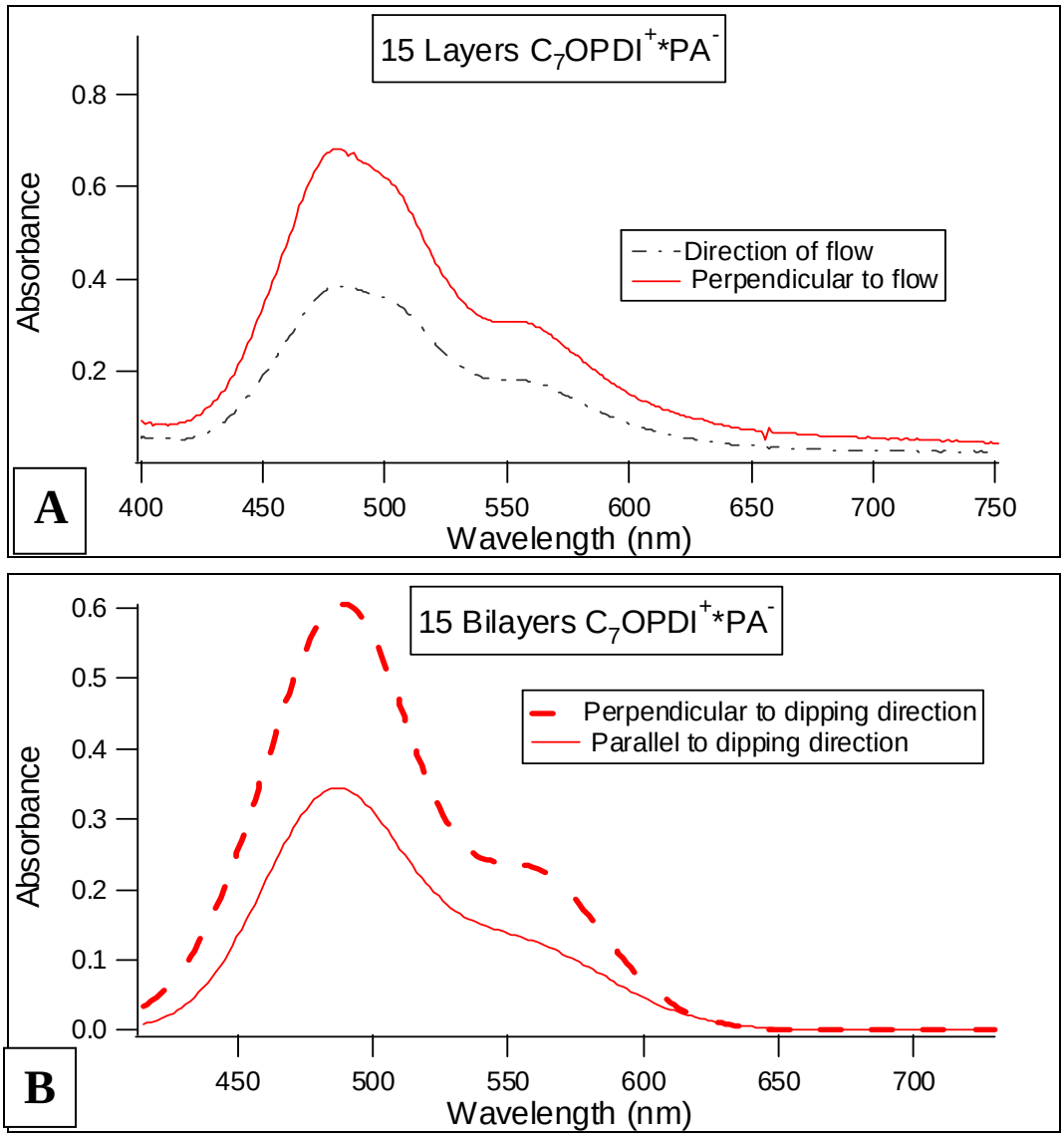

Figure 4.2. (A) Absorbance spectra of 15 bilayer thin film and (B) Absorbance vs. Bilayer Number

(A) Absorbance spectra of a 15 bilayer $C_7OPDI^+ \bullet PA^-$ composite film displaying the absorbance obtained with the light polarized in both parallel and perpendicular to the dipping direction. The peak maximum was 481 nm for both. (B) The absorbance as a function of bilayer number, both perpendicular and parallel to the dipping direction for the composites. The bilayers used in the 10, 15, 20, and 25 starting materials came from two different batches. The 30 bilayer sample came from one batch of starting material where only 2 samples were made. The other four bilayers had two samples made of this batch also.

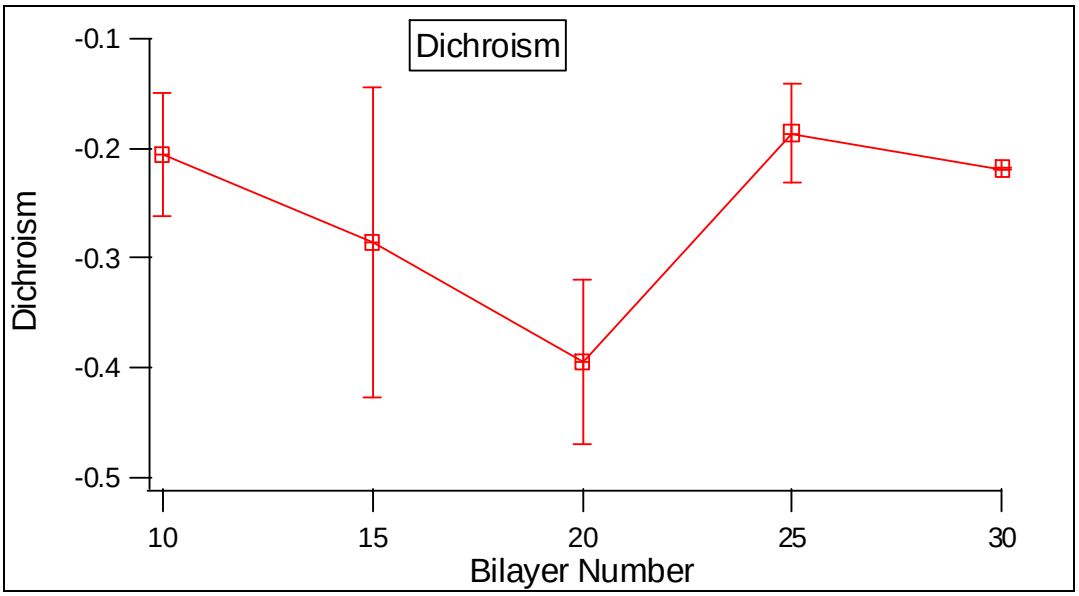

Figure 4.3. Dichroism vs. Bilayer Number

The average dichroism values were found as a function of bilayer number. Results from 4 samples were averaged together to find the D value for each film up to the 25 bilayer sample. The 30 bilayer sample only two thin films were made and used to find the average and standard deviation. The standard deviation is shown for each composite bilayer.

$$D = \frac{(A_{\parallel} - A_{\perp})}{(A_{\parallel} + A_{\perp})}$$

Equation 4.1. Dichroism

In the equation 4.1, D is the dichroism, $A_{\parallel}$ is the absorbance for light polarized parallel to dipping direction, and $A_{\perp}$ is the absorbance for light polarized perpendicular to dipping direction.

The dichroism of the films can be determined from the absorbance spectra. The equation used to figure out this dichroism is seen in equation 1. The dichroism was found to increase (in magnitude) slightly with bilayer number up to 20 bilayers, as seen in figure 3. Unfortunately, the dichroism did not increase as expected for 25 and 30 bilayer thin films. The loss of dichroism is due to the increase disorder. The mechanism for the fiber alignment will be explained later.

4.3.C. Morphology of the Composites:

The AFM was used to examine the surface morphology of the $C_7OPDI^+ \bullet PA^-$ thin films samples. The composites are clearly comprised of wavy thin fibers in the 10 and 15 bilayer composites, as shown in figure 4(A,D). These films gave an indication the fibers on the surface of the films were aligned in the deposition direction. However, not all the fibers on the film surface showed this alignment. The composite with 20 bilayers displayed thicker fibers as a result of smaller fibers grafting together, as seen in figure 4(C). The 25 and 30 bilayer composites showed loss of some of the fiber structure in favor of islands and the underlying film displayed an interconnected network. The island morphology explains the loss of dichroism observed in the 25 and 30 bilayer samples. The fiber structure is such where not all fibers display alignment in the deposition direction. The fibers appear to favor a vertical alignment over all, but there are also areas where alignment is not as evident.

The width of the fibers present on the film surface was found using image autocorrelation procedures.[10] Autocorrelation methods provided information on fiber width in both the vertical and horizontal direction. The fibers displayed an increase in fiber width with bilayer number as observed in figure 5(A). The films showed an increase in the width by a factor of 2 from the films with the fine fibers compared to the thicker composite films. A considerable difference between the widths in the vertical and horizontal directions is observed for fiber widths in some of the composites. The films with this large difference in width happen to be mostly from the films where fiber alignment is readily apparent from the UV-vis data. The width difference

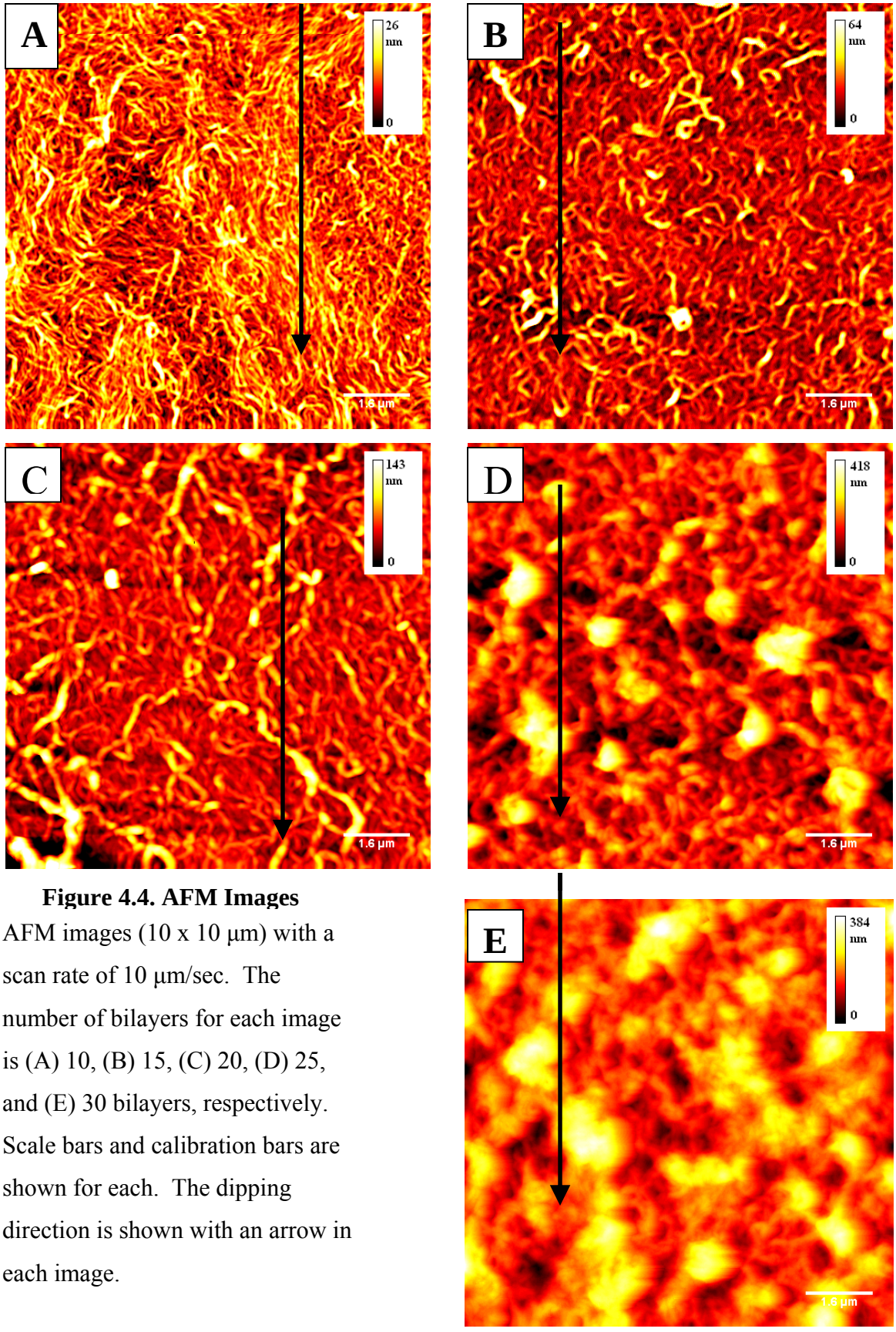

Figure 4.4. AFM Images

AFM images (10 x 10 µm) with a scan rate of 10 µm/sec. The number of bilayers for each image is (A) 10, (B) 15, (C) 20, (D) 25, and (E) 30 bilayers, respectively. Scale bars and calibration bars are shown for each. The dipping direction is shown with an arrow in each image.

between the vertical and the horizontal was found to decrease when the films reached the higher bilayer numbers. The higher bilayer number films displayed more fibers with large features connected to mounds, thus the reason for the loss of the difference is due to the formation of the mounds. The mounded features are the dominant reason for the fiber width of the 25, and 30 bilayer thin films being similar. The 20 bilayer thin film was similar, because of the long fibers in one of the directions.

The thickness of the films was examined to explore how the thickness varied with bilayer number, due to fiber growth. The films thickness shows some evidence that it increases with bilayer number, as displayed in figure 5(B). The thin films displayed a steady increase in film thickness for three of the five samples, with the 20 and 30 bilayers providing the exception. The decline in thickness at the 20 can be explained by the decline in the precursor concentration brought about by the previous trials. In the previous trials there was four samples made at each bilayer number before going on. After 20 bilayer composites were made, more of the precursor solution was added to increase the volume of solution in the beaker. This effectively increased the concentration closer to the original starting solution. The decrease in precursor concentration was of big concern here because there happened to be four samples made at each bilayer number, before going on to the next. This was in an attempt to see if the withdrawal speed effected alignment, however there was no change readily apparent. The decline in film thickness at the 30 bilayers can be explained by the sample used here being made from a different batch of the starting C_7OPDI^+.

The surface features observed by AFM were analyzed for the purpose of finding situations in which the fibers aligned along the deposition direction, as previously reported.[14] The process to determine fiber alignment involved finding the maximum second directional derivative and the direction of the maximum. The former yields the "Hessian ridges image" that better displays the fibers in the composite film, see figure 6(B). This image can be used to find any possible alignment of the fibrous features. Figure 6(C) gives a prime example of this where there happens to be a large occurrence of fibers aligned along the vertical direction. The fact that fiber alignment is not in the same direction as the AFM tip scan direction (horizontal) is of importance. This indicates the fibers are aligned during deposition and not by the tip dragging on the sample surface.

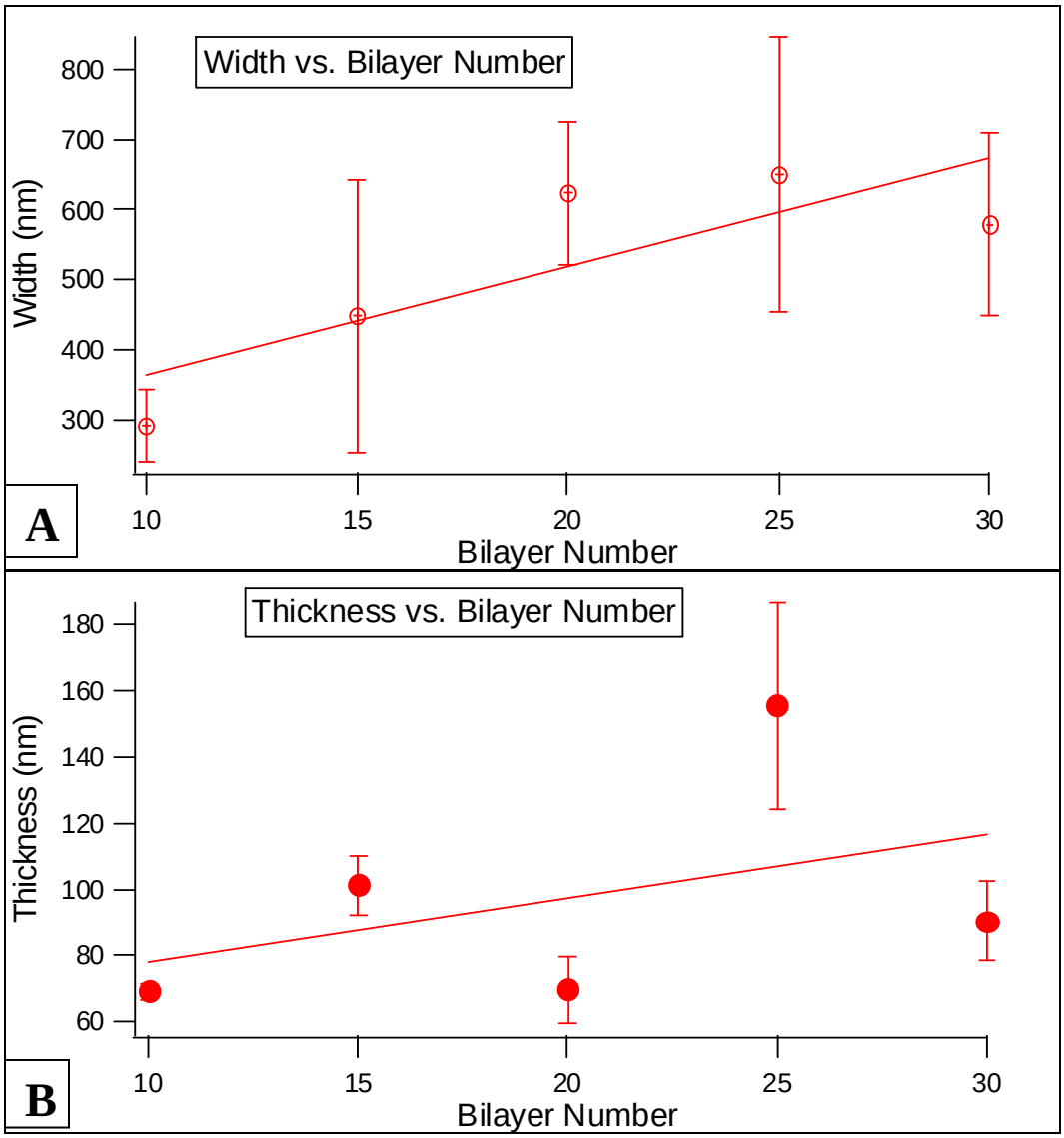

Figure 4.5. (A) Width of Fibers vs. bilayer number and (B) Thickness vs. bilayer number

(A) Average width of the fibers from three AFM images as a function of bilayer number. Two samples were imaged in each case. (B) Thickness of the composites as a function of bilayer number. The standard deviation is shown at each data point, determined from 3 replicate measurements.

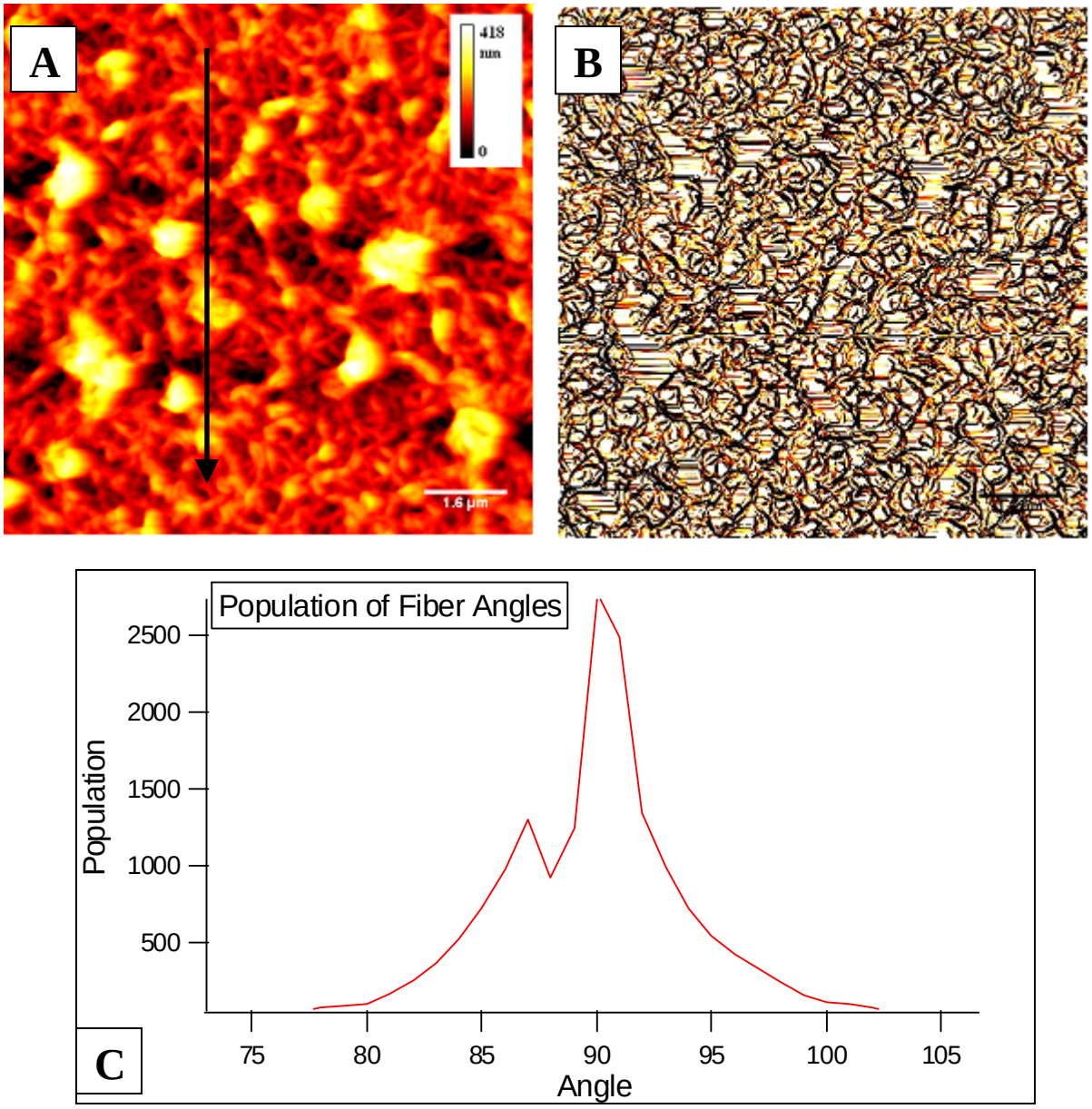

Figure 4.6. Population of Angles

(A) A 10 x 10 µm AFM image (10 µm/sec. scan rate) of a 25 bilayer composite displaying fiber alignment. An arrow is shown indicating the direction of deposition. (B) The same image showing the Hessian ridges image generated from the analysis program. (C) The histogram generated from the fiber analysis software. This histogram displays the population of fiber angles for this composite. This data shows there is a greater population of fibers aligned parallel to flow direction in this image. The direction of deposition was vertical on the substrate.

4.3.D. Mechanism of Aligned Fiber Growth:

The mechanism describing how the aligned fibers came about involves electrostatic-self-assembly. The initial aggregates deposited on the surface will act as nucleation sites for further growth. With the initial aggregates present on the surface causes the classical charge reversal on the substrate at that location, as often seen in LBL processes allowing for further nucleation.[12] Further nucleation occurs by deposition of the PE. The fibers continue to get longer and thicker with each deposition cycle. This leads to fibers overlapping and growing together with the possible loss of true fiber structures.

The substrate is held perpendicular to the solution surface. The deposition direction of the substrate was by inserting the substrate straight into the solution and pulled straight up in the withdrawal phase. When the aggregates deposit, the result is the fibers aligned parallel to the substrate dipping direction. These fibers are self aligned parallel to the deposition direction with the π-bonds of the PDI being perpendicular to the deposition direction.[10] Figure 7 shows how the aggregates go down with the π-bonds being perpendicular to the withdrawal direction. That the π-bonded PDI chromophores are perpendicular to the deposition direction is evidenced by the dichroism studies.

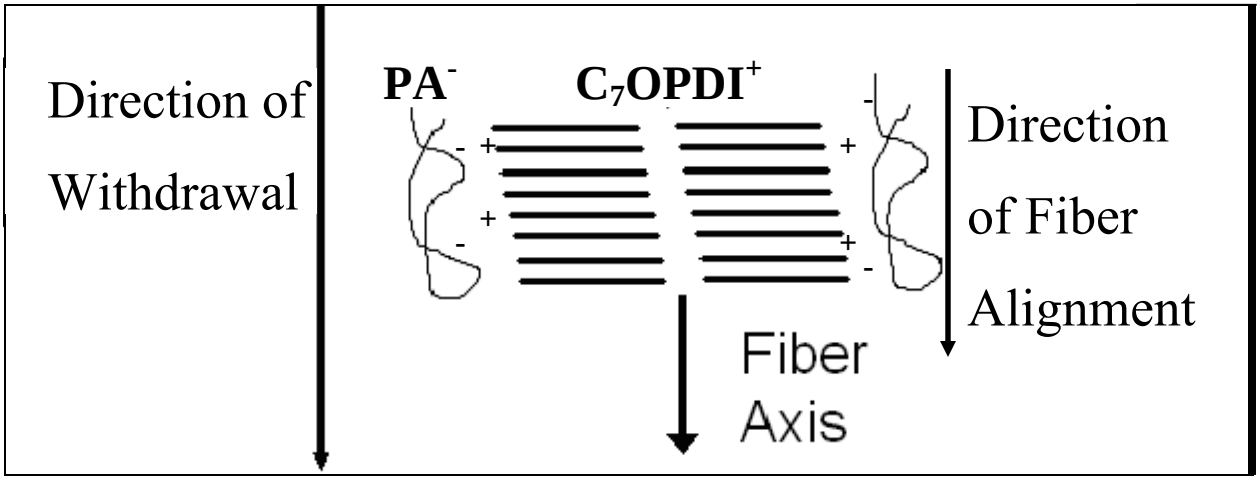

Figure 4.7. Model of mechanism

Model of how $C_7OPDI^+ \bullet PA^-$ composite is organized in the film. The model also displays the alignment in the deposition direction.

4.4. Conclusion:

ESA-based LBL deposition was used to prepare films of aligned $C_7OPDI^+ \bullet PA^-$ composites. These films incorporated fibers of the $C_7OPDI^+ \bullet PA^-$ composite with alignment in the bulk of the film parallel to the dipping direction. This alignment was readily evident in the dichroism studies. Alignment is not as readily observed in AFM images. The films and features present displayed the classic LBL growth in films thickness and feature widths. This readily shows the effects of charge reversal on the surface, creating larger and thicker features. This method has provided a way to grow aligned nanofibers in the bulk with several key advantages. The advantages of the process used here are the starting materials are water-soluble and an organic semiconducting material is incorporated. However, their needs to be further work to ensure all the fibers are in an aligned state. This method to produce aligned nanofibers could provide a means to produce organic semiconductor wires and control aggregate packing in organic thin film transistors.[15,16]

References:

[1] Gundlach, D. J.; Klauk, H.; Sheraw, C. D.; Kuo, C. C.; Huang, J. R.; Jackson, T. N. *1999 Tech. Dig. –Int. Electron Devices Meet.* **1999**, 111.

[2] Kluak, H.; Halik, M.; Zshieschang, U.; Schmid, G.; Radlik, W.; Weber, W. *J. Appl. Phys*. **2002**, 92, 5259

[3] Kelly, T. W.; Broadman, L. D.; Dunbar, T. D.; Muyres, D. V.; Pellerite, M. J.; Smith, T. P. *J. Phys. Chem. B* **2003**, 107, 5877

[4] Kelly, T. W.; Muyres, D. V.; Baude, P. F.; Smith, T. P.; Jones, T. D. *Mater. Res. Soc. Symp. Proc***. 2003**, 771, L6.5.1

[5] Yoo, B.; Jung, T.; Basu, D.; Dodabalapur, A.; Jones, B. A.; Facchetti, A.; Wasielewski, M. R.; Marks, T. *J. Appl. Phys. Lett*. **2006**, 88, 082104

[6] Weiss, E. A.; Ahrens, M. J.; Sinks, l.E.; Sinks, A. V.; Gusev, M. A.; Ratner, M. A. Wasielewski, M. R. *J. Am. Chem. Soc*. **2004**, 126, 5577.

[7] Tang, T.; Qu, J.; Müllen, K.; Webber, S. E. *Langmuir* **2006**, 22, 26.

[8] Xie, A.; Liu, B.; Hall, J.; Barron, J. L.; Higgins, D. A. *Langmuir* **2005**, 21, 4149

[9] Marcon, R. O.; Santos, J. G.; Figueiredo, K. M.; Brochsztain, S.; *Langmuir* **2006**,22, 1680.

[10] Everett, T. A.; Twite, A. A.; Xie, A.; Battina, S. K.; Hua, D. H.; Higgins, D. A. *Chem. Mater*. **2006**, 18(25), 5937.

[11] Decher, G. *Science* **1997**, 277, 1232.

[12] Balakrishnan, K.; Datar, A.; Oitker, R.; Chen, H.; Zuo, J.; Zang, L. *J. Am. Chem. Soc*. **2005**, 127, 10496.

[13] Marcon, R. O.; Santos, J. G.; Figueiredo, K. M.; Brochsztain, S. *Langmuir* **2006**, 22, 1680.

[14] Everett, T.E.; Higgins, D. A. (in publication)

[15] Hosoi, Y.; Tsunami, D.; Ishii, H.; Furukawa, Y. *Chem. Phys. Lett.* **2007**, 436, 139.

[16] Fujimoto, S.; Nakayama, K.; Yokoyama, M. *Appl. Phys. Lett*. **2005**, 87, 133503.

CHAPTER 5 - Conclusion

5.1. Conclusions:

A layer-by-layer (LBL) electrostatic-self-assembled (ESA) process was used to create mixed thin films from water-soluble perylene diimides (PDIs) and polyelectrolytes (PEs). PDIs used were N-(butoxypropyl)-N'-(2-(N,N,N-trimethylammonio)ethyl) perylene-3,4,9,10-tetracarboxylic diimide (C_7OPDI^+), bis (sulfonatopropyl) perylene diimide ($PDISO_3^{2-}$), and bis (trimethylammonioethyl) perylene diimide ($PDIDI^{2+}$), along with two PEs, poly(acrylic acid) (PA^-) and poly(diallyldimethylammonium chloride) ($PDDA^+$). The two symmetric PDI•PE composites displayed similar surface morphology with the difference being the $PDISO_3^{2-}$ •$PDDA^+$ composite had a more highly intertwined fiber morphology. The more heavily aggregated precursor solution of the C_7OPDI^+ when combined with PA^- resulted in wavy thin aligned fibers orientated parallel to the dipping direction. All the composites also displayed a change in the fibers appearance after 15 bilayers had been deposited in favor of fewer and thicker fibers from the result of the fibers growing together and overlapping. The C_7OPDI^+•PA^- composite had a film thickness approximately equal to the $PDISO_3^{2-}$•$PDDA^+$ composite, where the $PDDA^+$ has significantly higher molecular weight than the PA^-. All the PDI•PE composite thin films displayed the expected fiber width increase with bilayer number.

5.2. Future Work:

Future considerations designed for improved knowledge and understanding of water-soluble PDIs thin film growth are of several types. Both the PDI and PE solutions have several variables where adjustment would maximize understanding on thin film growth. The structure of the specialized PDIs investigated could be further modified for understanding of how the structure effects thin film growth. Real world tests of the current materials could be carried out.

The first consideration to be examined and the easiest is modification of the PE solution. First, determining the effects of lowering the concentration in the PEs solution changes the deposition rate the thin film growth. Second, how does varying in the ionic strength changes the deposition rate. This study would require trying several different ionic strengths with some as high as 10 M, thus a direct relationship on ionic strength to film thickness could be established.

Third, how changing the PEs molecular weight changes the films thickness. Fourth, how changing the temperature of the precursor solution affects the deposition rate of the thin films. Temperature effects on thin film forming properties might only be observed at temperatures near freezing. Temperatures higher than room temperature may not display any significant change in film formation.

PDI solutions have several variables worth modifying in consideration of increasing the alignment present in the thin films and for a better understanding of the deposition rate. Since the results presented in this thesis showed the PDI solution with the larger fraction aggregated resulted in alignment, the modifications here should be for increasing the aggregation present in the precursor solutions. The alignment here could be readily checked by absorbance dichroism studies. Modification number one is finding the effect of concentration on alignment in films. A higher concentration would have more aggregates present in solution and likely larger ones. The second modification is the effect of ionic strength on aggregation. High ionic strength would change the deposition rate of the PDIs and possibly result in formation of larger aggregates in solution. This would help determine the relationship of deposition rate on ionic strength. The final modification is the temperature of the precursor solution. The fraction aggregated would decrease at higher temperatures as a result of higher thermal motion.[1] At lower temperatures, slightly larger aggregates would be expected in the precursor solution. Temperature variations would allow for finding how a small change in aggregation affects the deposition rate.

Structural changes to the water-soluble PDIs would alter the thin film and surface features. Development of an asymmetric anionic water-soluble PDI could provide unique fiber structure, along with more heavily aggregated precursor solution. Lengthing of the carbon chains could provide interesting properties in thin film formation. Changing the length of the primary amines attached would be of interest in the two symmetrically charged PDIs. Branched tails should favor a more heavily aggregated solution, which would result in a different set of thin film growth conditions, and perhaps better alignment. These studies in thin film forming properties have the disadvantage of requiring synthesis of new compounds, which have not been prepared previously.

The most beneficial future work would be in investigating the semiconducting properties of the PDI•PE composites. The first experiment would be testing the thin films created in organic thin film transistors; PDIs have already been tested for these in the literature.[2,3] The

second test would be the effectiveness of PDI•PE composite as an active component of a photovoltaic device, where PDIs have already been tested before.[4] Photovoltaic testing would require the use of a p-type organic thin film as the substrate, allowing for deposition of the PDI thin film composite on top, thus an effective measure of the light harvesting efficiency could be obtained.

References:

[1] Balakrishnan, K.; Datar, A.; Naddo, T.; Huang, J.; Oitker, R.; Yen, M.; Zhao, J.; Zang, L. *J. Am. Chem. Soc*. **2006**, 128, 7390.

[2] Fujimoto, S.; Nakayama, K.; Yokoyama, M. *Appl. Phys. Lett*. **2005**, 87, 133503.

[3] Ling, M.; Bao, Z.; Erk, P.; Koenemann, M.; Gomez, M. *Appl. Phys. Lett*. **2007**, 90, 093508.

[4] Kudo, T.; Kimura, M.; Hanabusa, K.; Sharai, H. *J. Porhyrins Phthalocyanines* **1998**, 2, 231.